Earth Energy Science 1 (2025) 123–143

Contents lists available at ScienceDirect

Earth Energy Science

journal homepage: www.keaipublishing.com/en/journals/earth-energy-science/

Experimental insights into the nucleation and propagation of hydraulic fractures in anthracite coalbed methane reservoirs

Saipeng Huang[a,f,*], Dameng Liu[c], Enrique Gomez-Rivas[b], Albert Griera[d], Quan Gan[a], Mengyao Wang[a], Yin Xing[g], Yang Zhao[e]

[a] School of Resources and Safety Engineering, Chongqing University, Chongqing 400044, China
[b] Departament de Mineralogia, Petrologia i Geologia Aplicada, Facultat de Ciències de la Terra, Universitat de Barcelona (UB), c/ Martí i Franquès s/n, Barcelona 08028, Spain
[c] School of Energy Resources, China University of Geosciences, Beijing 100083, China
[d] Departament de Geologia, Universitat Autònoma de Barcelona, Bellaterra, Cerdanyola del Vallès 08193, Spain
[e] School of Petroleum Engineering, Northeast Petroleum University, Daqing 163318, China
[f] Hubei Key Laboratory of Resources and Eco-Environment Geology, Hubei Geological Bureau, Wuhan 430034, China
[g] School of Geography Science and Geomatics Engineering, Suzhou University of Science and Technology, Suzhou 215009, China

ARTICLE INFO

Keywords:
Hydraulic fracturing
Fracture propagation
Horizontal stress difference
Injection flow rate
Bedding orientation

ABSTRACT

Developing low-permeability Coalbed Methane (CBM) reservoirs can significantly benefit from a comprehensive understanding of hydraulic fracture nucleation and propagation mechanisms, particularly in anthracite CBM reservoirs. This study employs true-triaxial hydraulic fracturing experiments to investigate these mechanisms, with variables including injection flow rate, horizontal stress difference (σ_H-σ_h), and bedding orientation. Additionally, we conduct corresponding numerical cases to validate the experimental conclusions. The research also considers re-fracturing instances. For the first time, we utilize a combination of Kaiser tests and the stress transfer function in ANSYS Workbench finite element analysis to accurately restore the confining pressure of the coal sample. The findings suggest that a high initial injection flow rate during hydraulic fracturing can promote fluid leakage and aid in maintaining substantial fracture pressure. Enhanced fracturing efficiency can be achieved through higher injection rates, and it can ensure optimal fracturing efficiency, minimizing roof and floor fracturing in coal reservoirs to prevent fracturing fluid leakage. The presence of a high horizontal stress difference facilitates hydraulic fracture propagation along the direction of the maximum horizontal compressive stress, requiring a greater hydraulic pressure to produce more fracture systems in coal reservoirs. Additionally, a minor deviation in the wellbore injection direction from the bedding orientation assists in creating a complex hydraulic fractured network, although this also requires higher hydraulic pressure to initiate new fractures. In the case of multiple hydraulic fracturing, the second initiation pressure tends to be significantly higher than the first, indicating that a sequential increase in hydraulic pressure aids the formation of additional fractures. Moreover, a simplified numerical simulation has been conducted to corroborate the experimental findings. These insights are crucial in optimizing hydraulic fracturing processes to enhance the permeability of anthracite CBM reservoirs.

1. Introduction

Hydraulic fracturing is one of the most effective methods to improve reservoir permeability and, accordingly, has been widely used to stimulate oil and gas production for years, especially in low-permeability unconventional resource reservoirs such as coalbed methane, shale gas, and oil (Chen et al., 2013; Guo et al., 2014; Ulrich et al., 2018; Hu et al., 2020; Sherratt et al., 2021; Zhao et al., 2022a). The stimulation process generates new fractures and also propagates or causes sliding or opening of the existing ones, thus improving the connectivity of natural fracture networks, increasing reservoir permeability, and promoting the ability of the reservoirs to seepage (Huang et al., 2017; Zou et al., 2021). As the success of hydraulic fracturing directly impacts oil and gas production, (Liu et al., 2022) optimizing and improving this process

* Corresponding author at: School of Resources and Safety Engineering, Chongqing University, Chongqing 400044, China.
E-mail address: huangspcugb@hotmail.com (S. Huang).

https://doi.org/10.1016/j.ees.2025.01.002
Received 25 October 2024; Received in revised form 10 December 2024; Accepted 2 January 2025
Available online 28 January 2025

is of great importance (Lin et al., 2017; Taghichian et al., 2018; Iqbal et al., 2018; Vishkai and Gates, 2019). Numerous studies have focused on analyzing the factors that control hydraulic fracturing, e.g., including fracturing methods (such as multi-stage fracturing, acid fracturing, diversion techniques, etc.), the type of fluids involved, the reservoir characteristics, the *in situ* stress orientation and magnitude, and the presence of pre-existing natural fractures, among others (Bredehoeft et al., 1976; Bohloli and Pater, 2006; Shimizu et al., 2011; Liu et al., 2018; Wei et al., 2020; Zhao et al., 2021). Among these factors, predicting the effect of *in situ* stress on hydraulic fracture propagation is particularly challenging because estimating the *in situ* stress in the subsurface is a difficult task. The hydraulic fracturing (HF) method has been proven to be an effective approach for measuring *in situ* stress, as demonstrated by Haimson and Cornet (Haimson and Cornet, 2003) and Zhang and Roegiers (Zhang and Roegiers, 2010). On the other hand, the Kaiser test is known for its advantages in terms of easy use, low cost, and is an effective method to estimate *in situ* stress compared to the HF method (Kaiser, 1953; Lehtonen et al., 2012). The Kaiser test is based on the Kaiser effect, by which a rock emits elastic waves when it is subjected to stress, but when stress ceases and the rock is reloaded, the acoustic emission will only occur when the stress surpasses the previous level of stress that was applied (Lehtonen et al., 2012).

In situ stress is a crucial factor that controls hydraulic fracturing in coal seam reservoirs (Wang et al., 2021a). It is generally assumed that hydraulic fractures tend to propagate along or nearly parallel to the direction of the maximum principal stress (Laubach et al., 2004). However, this behavior can be more complicated in some systems (see the review of natural hydrofractures by Bons et al. (2022)).). For example, the presence of bedding planes and other discontinuities, such as pre-existing natural fractures, can affect the initiation and propagation paths of newly generated hydraulic fractures (Grasselli et al., 2015; He and Duan, 2019). Simulations by Zou et al (Zou et al., 2016). revealed that high injection pressures are required to create hydraulic fractures when bedding planes are present in shale reservoirs. Furthermore, 2D numerical simulations by Ohtani et al (Ohtani et al., 2017). showed that hydraulic fractures tend to propagate along the maximum principal stress orientation when the differential stress is relatively large (e.g., 5.0 MPa), while they tend to propagate along bedding planes under lower differential stress in shale reservoirs (for example, below 2.5 MPa in their study), these discontinues promote preferential paths for fracturing.

To ensure successful coalbed methane production, it is essential to understand how the regional stress field is locally resolved (Ju et al., 2018). Unravelling the orientation and magnitude of the principal stresses is crucial for predicting the propagation direction of hydraulic fractures. The problem of the influence of the stress field orientation on coal-bearing hydrocarbon reservoirs has also been tackled by means of laboratory rock deformation experiments (Liu et al., 2021). Additionally, the stress field orientation can be predicted based on the coal reservoir's cleats and natural fractures. For instance, Paul and Chatterjee (Paul and Chatterjee, 2011) conducted a study where they gathered the orientation of cleats and fractures from coal exposures and underground coal mines, then further compared these orientations with the *in situ* stress data that had already been acquired. Their analysis revealed that the maximum horizontal stress direction was similar to that of the face cleat orientation.

In addition to the stress field, several other factors have been identified as important in determining hydraulic fracturing behavior. For instance, Liu et al (Liu et al., 2018). conducted true-triaxial fracturing experiments and found that the approaching angle, which is defined as the angle between a pre-existing natural fracture and the maximum horizontal principal stress, determines whether a hydraulic fracture propagates along the pre-existing natural fracture. Conversely, earlier work by Liu et al. (2014). showed that hydraulic fractures tend to propagate along the path of least resistance and shortest distance, illustrating how reservoir anisotropy affects fracture propagation. Similarly, the angle at which shear fractures nucleate can be significantly influenced by the presence of anisotropy (Gomez-Rivas and Griera, 2012). Furthermore, Zhao et al. (2022b). demonstrated that the initiation pressure of the reservoir decreases with the increasing injection rate in shale reservoirs. Moreover, the use of low-viscosity fluids accelerates fluid access into the fracture (Shimizu et al., 2011).

Numerous studies have been conducted on the formation of hydrofractures, mostly through numerical modeling, experiments, and analysis of hydraulic fracturing field data such as micro seismicity (Shimizu et al., 2011; Liu et al., 2018; Wang et al., 2017; Huang et al., 2019; Lyu et al., 2020). For example, Wang et al. (2017). explored the impact of natural fractures on coal hydraulic fracturing using numerical modeling, while Huang et al. (2019). demonstrated the utility of microseismicity data for identifying the direction of hydraulic fracture propagation. However, there has been limited experimental research on anthracite coal in CBM reservoirs, drawing attention to key factors such as natural fractures, *in situ* stress, and injection flow rates (Liu et al., 2018). Notably, current studies do not generally consider that the injection flow rates can frequently vary in hydraulic fracturing sites, while most experimental studies use a fixed injection flow rate. Additionally, while most hydraulic fracturing experiments focus on vertical well fracturing, horizontal well fracturing is now more commonly used to stimulate reservoirs. Moreover, since coal samples are typically covered with a layer of cement during experiments to prevent them from breaking apart, the stress transfer from confining stress loading on the cement surface is often neglected, (Mou et al., 2021; Zhao et al., 2022c; Pan et al., 2022) which can introduce bias into the experimental results. To address the challenges above and achieve a deeper understanding, it is crucial to undertake a comprehensive assessment of the various factors that impact hydraulic fracturing in anthracite reservoirs.

Accordingly, this experimental study aims to gain more insights into hydrofracture formation in anthracite coal of CBM reservoirs by investigating the effects of the complex *in situ* stress distribution, injection flow rates, and bedding plane orientation on hydraulic fracturing. The study is based on samples and data from the Zhengzhuang block of southern Qinshui Basin (SQB). Specifically, we aim to determine (1) how the *in situ* stress distribution affects hydraulic fracturing, (2) how different injection flow rates impact hydraulic fracture propagation, and (3) how bedding plane orientation influences the direction of hydraulic fracture propagation. Hence, we regard the differential horizontal stress, injection flow rate variation, and bedding orientation as crucial factors that significantly influence the effectiveness of hydraulic fracturing. To accurately restore the confining pressure of the coal sample, we employ a combination of Kaiser tests and the stress transfer function using the finite element analysis. Furthermore, we incorporate re-fracturing in our experiments, a leading stimulation technology in oil and gas development, (Wei et al., 2020; Sun et al., 2019) and we use horizontal well fracturing to replicate field conditions. Finally, a series of hydro-mechanical simulations were done to validate our observations from experiments.

2. Geological background

The No. 3 coal seam of the Shanxi Formation is one of the most continuous and stable coal seams of the SQB, with relatively high gas content of 10–37 m^3/t (Zou et al., 2010; Wang et al., 2016). The burial depth of the No. 3 coal seam ranges from 300 to 1300 m in the Zhengzhuang block, (Huang et al., 2019) and the thicknesses of this seam is 3–7 m, which reveals that it is a potential CBM block in the SQB (Teng et al., 2015). The Zhengzhuang block experienced periods of compression at least three times during the Indosinian (~250 Ma), Yanshan (~208 Ma), and Himalayan (~65 Ma) periods, respectively (Huang et al., 2019; Cai et al., 2011; Chen et al., 2018). Owing to these orogenies, normal faults with a strike of NE–SW are also observed (Wang et al., 2021b). The No. 3 coal seam in the Zhengzhuang block contains many faults (Fig. 1), and can be characterized as a typical

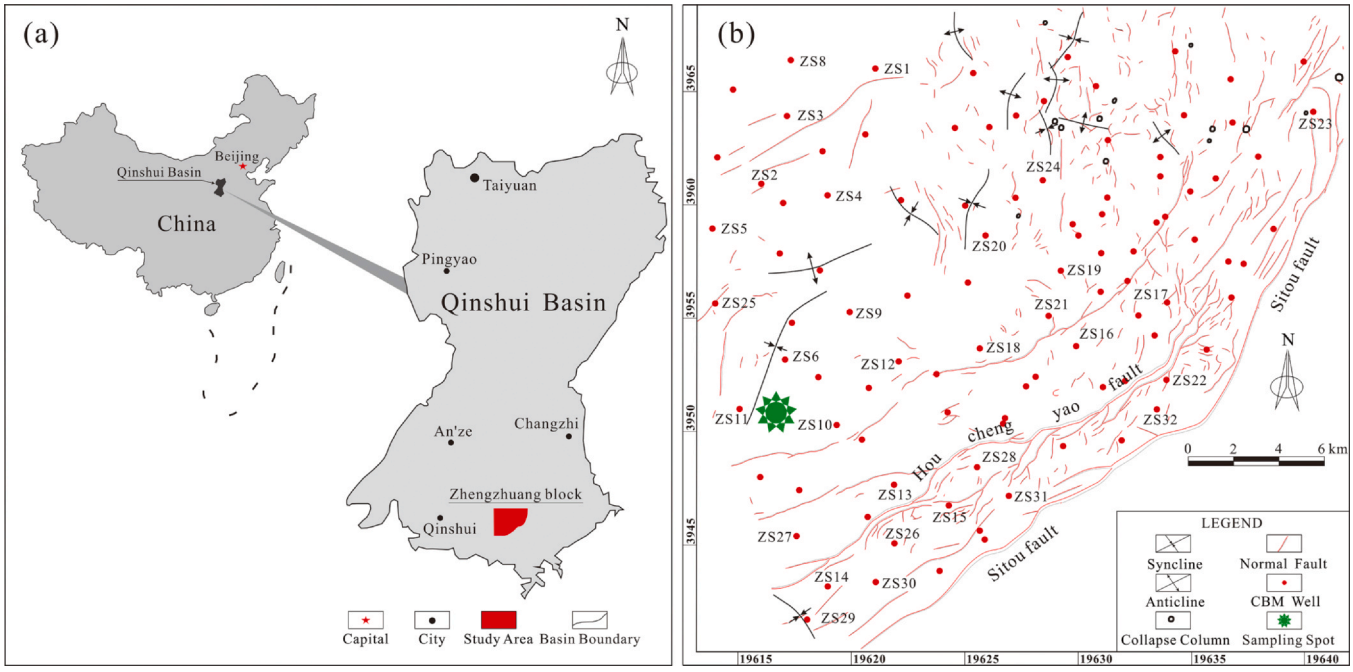

Fig. 1. (a) Location of Qinshui Basin in north China and the detailed study area in SQB; (b) The geological faults in Zhengzhuang block, and showing the sampling spot.

high-rank coal with maximum vitrinite reflectance (R_o) values ranging between 3.51% and 3.69% (Chen et al., 2018; Li et al., 2016). The coal samples selected for the fracture experiments were collected from the Qincheng coal mine, in the western of the Zhengzhuang block. According to Tingay et al. (2009), the pore fluid pressure in the reservoir can be classified into three categories worldwide, including mild (11.5–14.0 MPa/km), moderate (14.0–17.0 MPa/km), and high (> 17.0 MPa/km), respectively. The average formation pore pressure gradient is 9.1 MPa/km in the Zhengzhuang block, far below the lower boundary of 11.5 MPa/km of the mild category, which is slightly under-compaction compared with the theoretical hydrostatic pressure of 9.8 MPa/km. In addition, the formation pore pressure near the Qincheng coal mine varies from 3.49 to 3.59 MPa, (Huang et al., 2019) indicating that the coal samples were under-compaction.

3. Experimental and numerical materials and methodology

3.1. Experimental apparatus and setting

The experiments were carried out with a true-triaxial hydraulic fracturing apparatus at the China University of Petroleum (Beijing) (Fig. 2); this true-triaxial testing equipment is identified as a rigid platen type, and only cubic samples can be used. However, the three principal stresses loaded to cubic samples are limited to one orientation respectively, which cannot avoid the concentration of stresses at the sample edges. This problem can be greatly improved when the cylindrical specimen is used, and the new setup proposed by McDermott et al. (McDermott et al., 2018). can create principal stresses from multiple directions. Although this is a conventional apparatus with a function that only can realize mechanical (M) and hydraulic (H) processes, it enables stable loading of subsurface in-situ stresses and conducts hydraulic fracturing experiments.

The apparatus consists of a hydraulic voltage stabilizer, a true-triaxial rig, isolating rigs for the fracturing fluid and power oil, a servo-supercharger, a servo-hydraulic pump, and a data acquisition system (Huang et al., 2017). Pure water was used as the pore fluid to induce fractures in the experiments. The apparatus frame uses a flat jack to apply a rigid load to the sides of the cubic specimen. Three pairs of flat jacks were applied to simulate the principal vertical stress (σ_v), the maximum principal horizontal stress (σ_H), and the minimum principal horizontal stress (σ_h) separately. The coal sample was fixed on the plate, while the top and the sides of the sample were enclosed by pressure plates during hydraulic fracturing. The hydraulic fracturing fluid pressure comes from the servo-hydraulic pump and is supplied to the flat jack by a multi-channel pressure stabilization source. The computer can control each channel's pressure level separately, with a maximum supply pressure of up to 27 MPa for each channel. The pure water with tracer was driven by oil pressure and injected into the coal sample to promote the hydraulic fracturing process. All the experimental data are automatically recorded by the data acquisition system. Different conditions (Table 1) were considered during the series of hydraulic fracturing experiments to study the fracture initiation and propagation and further evaluate the factors affecting the effectiveness of fracturing in the coal seam.

Four samples were used, with labels A, B, C, and D. Every sample corresponds to a different experimental condition (Table 1). The coal samples were cut to a size of 200 × 200 × 200 mm and then encased with cement up to a size of 300 × 300 × 300 mm, following the same approach widely used in many previous studies (Liu et al., 2018; Mou et al., 2021; Zhao et al., 2022c; Pan et al., 2022). Different ratios of quartz sand and cement sand were tested to simulate various rock properties. Hence, a specific ratio has been chosen to ensure that the artificial cement meets the mechanical requirements for the roofs and floors in coal reservoirs (Fig. 3). Encasing the coal sample in cement offers several advantages. First, it effectively addresses the issue of anthracite coal being prone to crushing by creating a protective barrier around the sample. This isolation from direct pressure applied for the stiff plate helps prevent nucleation and fractures caused by factors unrelated to hydraulic fracturing. However, the study conducted by Fan et al. (2014)). does not consider this influence. Second, the presence of the cement layer allows the simulation of the roof and floor or interlayer typically found in coal reservoirs (Hu et al., 2020; Li et al., 2014) and, as such, we also explore the fracture propagation patterns within the roof and floor of the coal reservoirs.

The detailed process of making this encasement consisted of (1) on-site coal mine sampling, (2) coal sample cutting and processing

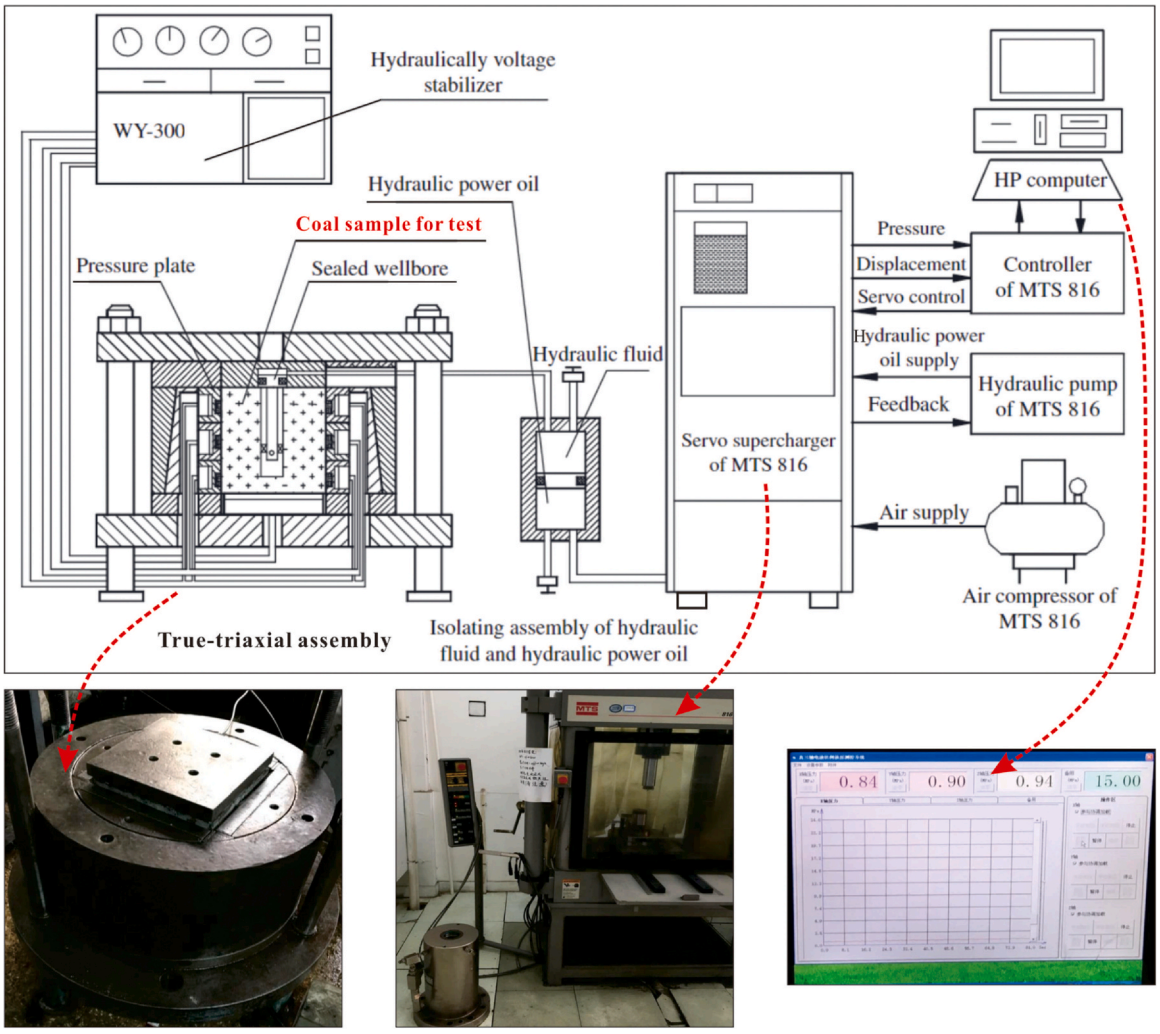

Fig. 2. Sketch of the true-triaxial hydraulic fracturing experimental apparatus used in this study (modified from Zhou et al. (2008).

(Figs. 3a and 3b), (3) indoor preparation of the cement, pouring cement to wrap coal samples in special containers (Figs. 3c), (4) drilling of boreholes with a drilling rig, (5) drying until the sample shape was fixed (Fig. 3d). A series of tests were conducted to obtain the necessary parameters for the experiments. Specifically, Kaiser tests were done to obtain the principal horizontal stress for the experiments. Brazilian splitting tests to obtain the tensile strength and conventional triaxial tests to obtain Young's modulus (E), Poisson's ratio (μ), density, compressive strength, friction angle, and cohesion, which can be used for numerical simulations purposes.

3.2. Kaiser tests and restoration of confining pressure

The Kaiser test is a highly effective method for accurate in-situ stress measurements (Kaiser, 1953; Lehtonen et al., 2012). Therefore, these tests were used to estimate the principal horizontal stress in the coal reservoir of the Qincheng coal mine and to set the confining pressure for the hydraulic fracturing experiments. Theoretically, the stress obtained from the Kaiser test represents the confining pressure that needs to be applied directly to the coal sample. However, in our experiments, the coal sample is covered with a layer of cement. Loading the Kaiser stress directly onto the cement would decrease the actual stress transferred to the coal sample, located 50 mm away from the cement surface, due to stress transfer effects. Numerical simulations were conducted to account for the reduction of stress values resulting from stress transfer, and to calculate the actual confining pressure that should be applied to the cement surface. This approach ensures a more precise restoration of the stress values and improves the reliability of the experimental results.

The confining stress reduction is restored by utilizing the stress transfer function in ANSYS Workbench finite element analysis. The

Table 1
Hydraulic Fracturing experimental conditions.

Sample No.	Injection flow rate (ml/s)	Wellbore orientation	Bedding plane orientation (°)	Loading conditions		
				σ_H (MPa)	σ_h (MPa)	σ_v (MPa)
A	0.30	Vertical	0	10.66	10.05	13.66
B	0.30–0.60	Vertical	30	10.66	10.05	13.66
C	0.60	Horizontal	90	15.99	15.07	13.66
D	0.30	Vertical	0	15.99	15.07	13.66

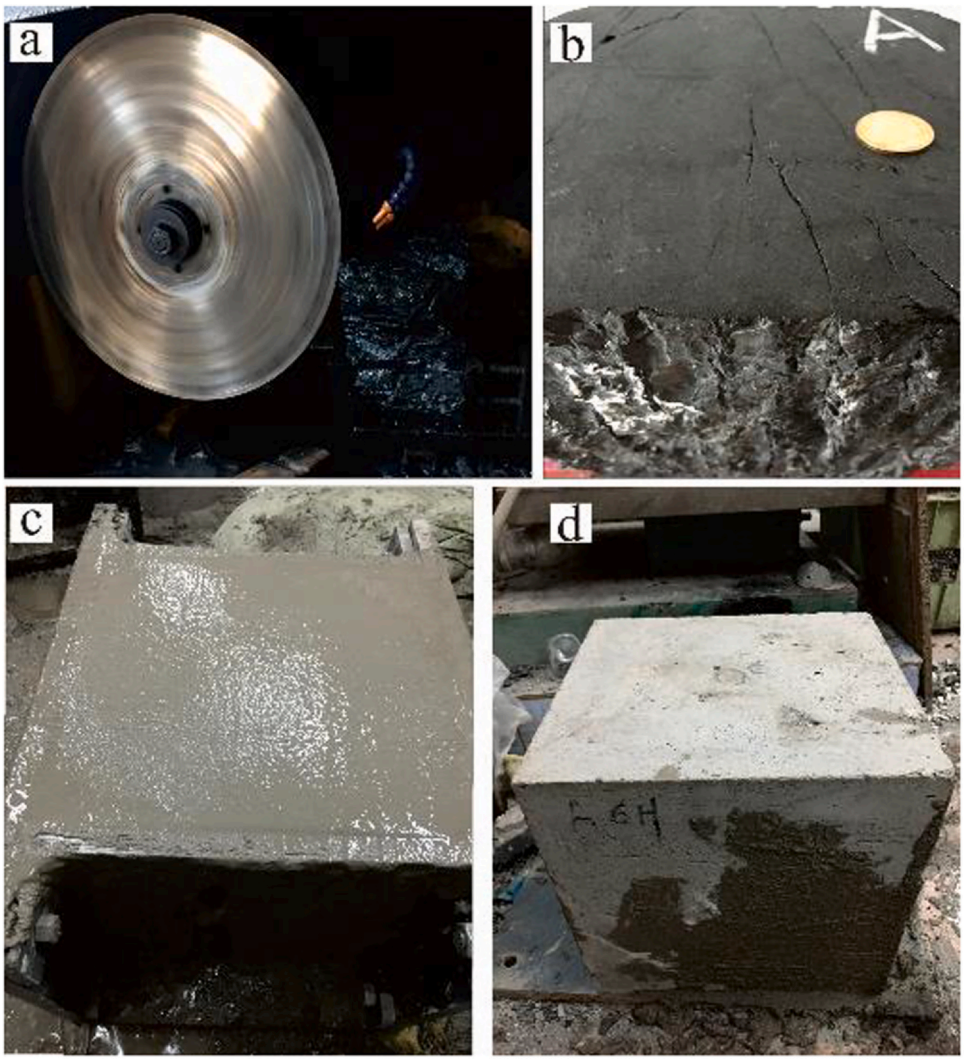

Fig. 3. Process for sample preparation. (a) Coal sample cutting and processing; (b) marking samples; (c) indoor preparation of the encasing cement, pouring cement to wrap coal samples in special containers; (d) drilling boreholes, drying until the sample shape is fixed.

detailed simulation process is as follows: (1) A cube model was established with the size of 300 × 300 × 300 mm, similar to the experimental sample size, thus restoring the experimental environment; (2) the model was meshed using tetrahedron elements with a resolution of 0.006 m; (3) the stress path was defined by three directions of the σ_H, σ_h, and σ_v, respectively; (4) the loading stresses were varied from 5 to 15 MPa based on the results from the Kaiser tests where the obtained values were less than 15 MPa; (5) after the post-processing, based on the simulation results, the formulas were fitted to calculate the stresses at 50 mm from the sample boundary. Consequently, the approach can be used to back-calculate the stress magnitude that needs to be loaded onto a 300 × 300 × 300 mm specimen using the principal horizontal stress obtained from the Kaiser tests.

3.3. Protocol for hydraulic fracturing experiments

According to the purpose of the study, different experimental protocols were designed for samples A, B, C, and D. Fig. 4a shows the size of the coal sample, cement, and wellbore. For sample A, the wellbore is perpendicular to the bedding orientation of the sample (Fig. 4b). The experimental variables are shown in Table 1. Fresh water was adopted as a fracturing fluid, and a fluorescent tracer was added. The injection flow rate was maintained at 0.30 ml/s, and the change in the oil pressure curve was monitored. The fracturing fluid was continuously injected until filtration loss occurred.

The bedding orientation of sample B was set at 30° to the horizontal direction (Fig. 4c). The loading conditions were similar to those of sample A. The injection flow rate was kept at 0.30 ml/s during the hydraulic fracturing experiment until the oil pressure peaked. To achieve dynamically changing flow rates during hydraulic fracturing, the injection flow rate rapidly increased when the oil pressure began to decrease. Specifically, the flow rate was adjusted from 0.30 ml/s to 0.60 ml/s within a span of 5 seconds. This approach ensured that the oil pressure exhibited an increasing trend while facilitating the desired variations in flow rates.

Sample C was designed to simulate the fracturing of the horizontal well by loading σ_H in the vertical direction (Fig. 4d). The wellbore was parallel to the bedding direction. The injection flow rate was set to 0.60 ml/s. The last sample D loading condition was set as sample C's. The wellbore was perpendicular to the bedding (Fig. 4e). The initial injection flow rate was 0.30 ml/s.

In addition, as in many previous hydraulic fracturing experiments, the sample was opened immediately after the experiment finished to observe the hydraulic fractures inside the sample (Huang et al., 2017; Liu et al., 2018; Zhou et al., 2008). However, many studies ignored the characteristics of the fracture distribution formed on the cement boundary surface of the sample as the roof and floor during the hydraulic fracturing process (Mou et al., 2021; Zhao et al., 2022c; Pan et al., 2022). In this study, the fractured sample was observed in two

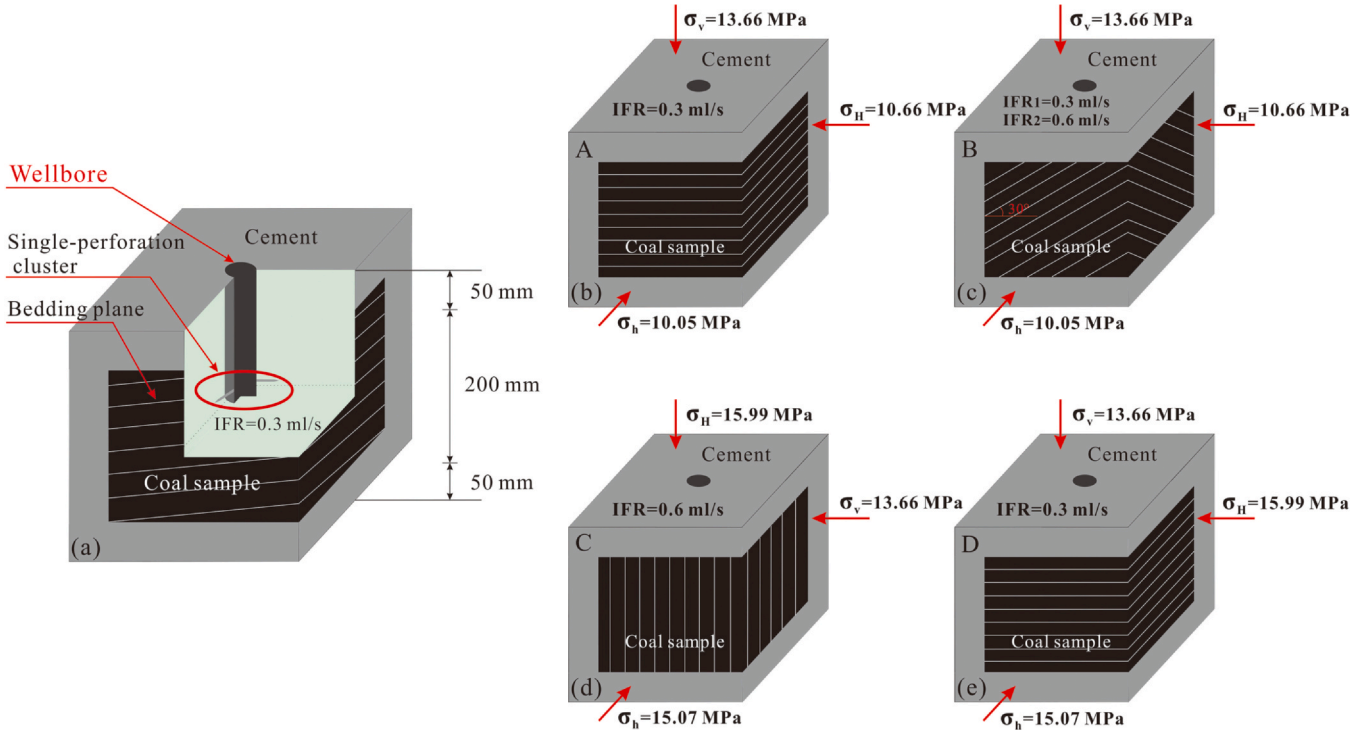

Fig. 4. Schematic diagram of the hydraulic fracturing experimental conditions. (a) Sketch of fractured sample; experimental setup of samples (b) A, (c) B, (d) C, and (e) D. The red arrows depicted in figures (b), (c), (d), and (e) signify the directions of the applied confining pressure.

steps to analyze the experimental results further. First, the six boundary surfaces of the sample were numbered and photographed to evaluate the distribution of fractures after the experiments. Second, the samples were opened to observe the distribution of hydraulic fractures near the wellbore. All four samples underwent two rounds of hydraulic fracturing to simulate re-fracturing technology. The initiation pressures for each round were collected from the time-oil pressure curves and analyzed.

4. Results

4.1. Coal sample mechanical properties

Two sets of coal samples from the Qincheng coal mine in the Zhengzhuang block were collected along the horizontal and vertical directions of the coal seam, and Brazilian split tests were carried out on samples of QCV-1 and QCH-1. The Brazilian test results of samples QCV-1 and QCH-1 are shown in Table 2. The tensile strength ranges from 1.38 to 1.62 MPa, showing that the tensile strength in the vertical direction is higher than that in the horizontal direction, indicating the mechanical properties of the coal reservoir are close to anisotropic. The compressive strength was obtained under different confining pressures (Table 3). The Biot coefficients were tested for the coal samples of the Qincheng coal mine, and the results differ significantly (Table 4). Two sets of coal cores, each in the 0°, 45°, and 90° to the horizontal orientation of the coal seam, were taken according to the standard coring procedure for the Kaiser test (Kaiser, 1953; Lehtonen et al., 2012). The principal horizontal stress of the coal samples is summarized in Table 5. The obtained σ_H and σ_h in the Qincheng coal reservoir are 9.75 MPa and 9.27 MPa, respectively, while σ_v is 12.72 MPa.

Table 2
Brazilian split test results.

Sample No.	Diameter (mm)	Thickness (mm)	Damage loads (N)	Tensile strength (MPa)
QCV−1	24.96	6.8	433	1.62
QCH−1	24.92	7.28	392	1.38

4.2. Restoring confining pressure

Table 6 shows the mechanical parameters of quartz sand and cement sand with different ratios tested in the laboratory. The chosen ratio of quartz sand to cement sand was 1:0.8. Hence, the rock mechanical parameters associated with this cement ratio are applied in the stress conduction simulation. In this paper, Young's modulus, E, Poison's ratio, μ, and the tensile strength were given as 16.28 GPa, 0.15, and 4 MPa, respectively; more details are shown in Table 6. We built a 300 × 300 × 300 mm cement model according to the size of the coal sample and applied stresses on the x, y, and z axes, respectively. The boundary conditions of the model are defined as shown in Fig. 5a. All loadings were applied by surface effect. Displacement in each surface was constrained along the directions of the x-axis, y-axis, and z-axis, respectively (see more details by Huang et al (Huang et al., 2017)). Thus, the cement model was considered linearly elastic and isotropic according to Silva and Einstein (Silva and Einstein, 2014).

After post-processing, the equivalent stress is derived from the middle surface of the model along the x-axis, as shown in Fig. 5b. The σ_H, σ_h, and σ_v, at a distance of 50 mm from the sample boundary, were simulated for loading conditions of 5 MPa, 7.5 MPa, 10 MPa, 12.5 MPa, and 15 MPa, respectively. The simulation results show the stress values at 50 mm from the loading boundary in Figs. 6b, 6d, and 6f. The σ_H and σ_h in the Qincheng coal reservoir obtained from the previous Kaiser tests were 9.75 MPa and 9.27 MPa, respectively, and σ_v was 12.72 MPa. The values of σ_H, σ_h, and σ_v calculated from numerical simulations to load onto the surface of samples A and B were 10.66 MPa, 10.05 MPa, and 13.66 MPa, respectively, with a lateral pressure coefficient of 0.758. The loading to samples C and D were σ_v = 13.66 MPa, σ_H = 15.99 MPa (σ_H was applied to the vertical direction of the sample), and σ_h = 15.07 MPa, respectively, with lateral pressure coefficient of 1.137.

Table 3
Results of conventional triaxial experiments.

Sample No.	Length (mm)	Diameter (mm)	Weight (g)	Density (g/cm^3)	Confining pressure (MPa)	Compressive strength (MPa)
QC−1	50.60	24.88	39.07	1.59	3.60	31.01
QC−2	42.54	24.86	29.29	1.42	7.20	30.05

Table 4
Biot Coefficient measurement results.

Sample No.	Length (mm)	Diameter (mm)	Density (g/cm^3)	The skeleton bulk modulus (MPa)	Particle bulk modulus (MPa)	Biot Coefficient
QC−3	50.6	24.88	1.59	10630	4510	0.58
QC−4	42.54	24.86	1.42	12370	3120	0.75

Table 5
Results of the Kaiser test.

Sample No.	Kaiser point	tan2β	σ_H (MPa)	σ_h (MPa)	σ_v (MPa)
QC1–0°	7.43	0.10570236	9.75	9.27	12.72
QC1–45°	6.43				
QC1–90°	6.95				
QC2–0°	6.77	−0.0573566	8.31	6.79	8.94
QC2–45°	6.36				
QC2–90°	5.26				

Table 6
Mechanical parameters of quartz sand and cement sand in different proportions.

No.	Ratio	Diameter (mm)	Length (mm)	Weight (g)	Density (g/cm^3)	Damage strength (MPa)	E (GPa)	μ
1	1:0.2	24.65	54.52	52.39	2.01	72.34	14.38	0.20
2	1:0.4	24.61	51.74	52.24	2.12	60.02	13.78	0.14
3	1:0.6	24.43	53.08	51.00	2.05	49.98	12.04	0.16
4	1:0.8	24.25	56.85	56.14	2.14	60.30	16.28	0.15

Ratio = Quartz sand/cement sand.

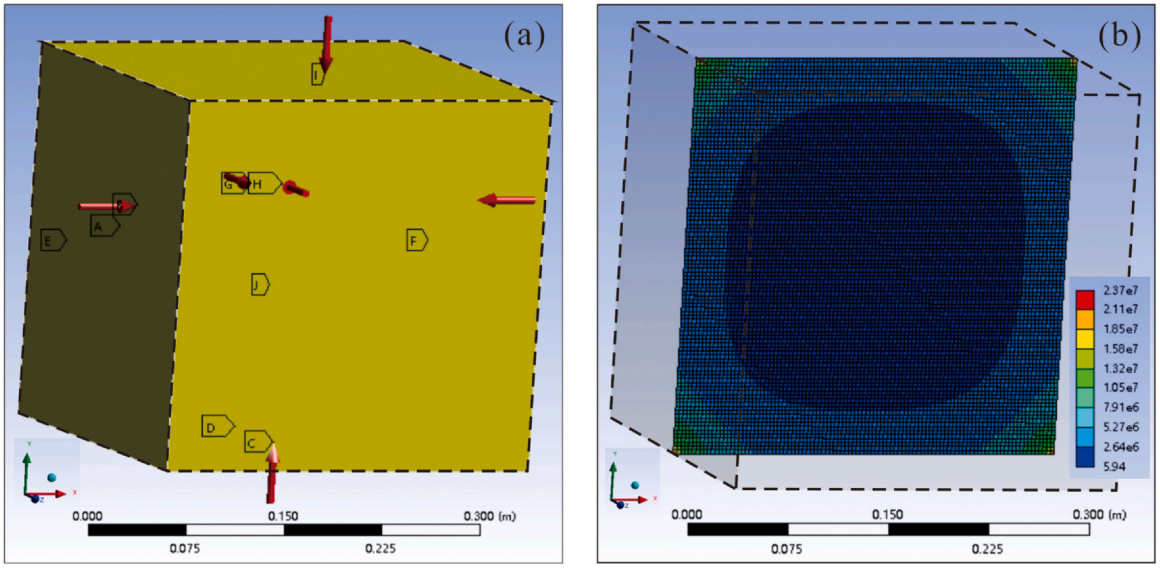

Fig. 5. (a) The geometric and boundary conditions of the model; (b) Equivalent stress is derived from the middle surface of the model along the x-axis. The color bar units are Pa.

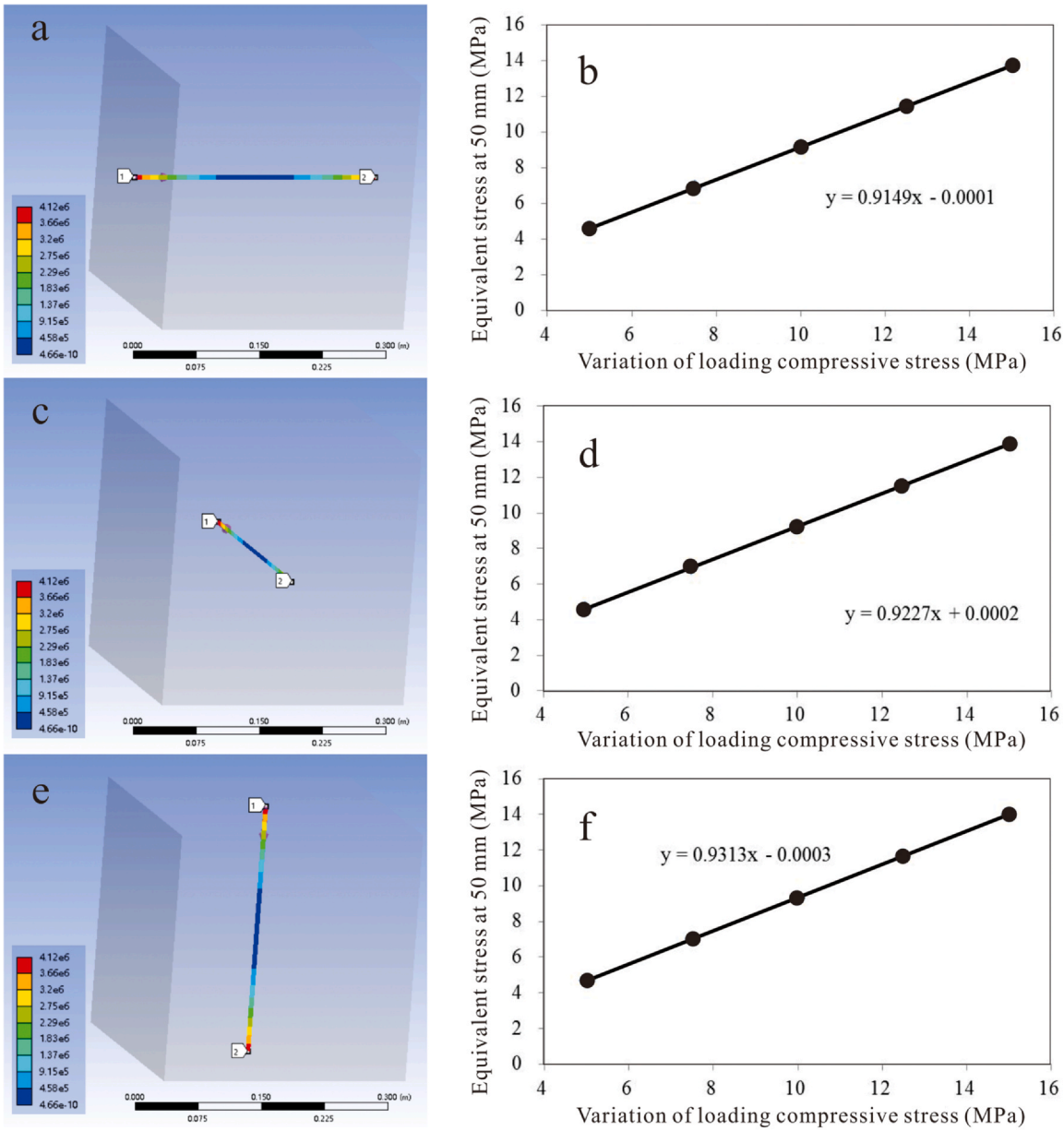

Fig. 6. (a), (c), and (e) Simulation of the equivalent stress path of σ_H, σ_h, and σ_v, respectively. For this case, the loading confining stress is 5 MPa; (b), (d), and (f) show the corresponding results of each simulation of the equivalent stress at 50 mm from the loading boundary. The units in the color bars are in Pa.

4.3. Dynamic monitoring of hydraulic fracturing pressure

The hydraulic fracturing fluid pressure generally varies rapidly with the hydraulic fracturing process, indicating the reservoir's initiation pressure (breakdown pressure) (Huang et al., 2017). Therefore, each sample's oil pressure *vs.* time curve is analyzed and compared. The oil pressure serves as an indicator of the hydraulic pressure within the fractures.

The time-displacement curve of sample A shows that the loading rate was kept at a breakneck speed during the first 14 minutes of hydraulic fracturing and then remained paused from 14 to 38 minutes (Fig. 7a). The corresponding time-oil pressure curve indicates that oil pressure reached a maximum of 6 MPa at the beginning of hydraulic fracturing (marked by the circle in the figure) and then dropped rapidly, meaning that the coal rock underwent hydraulic failure in the first instance. Then, the oil pressure began to decrease with a pause in the loading displacement until it remained at around 0.6 MPa (Fig. 7b). In the second stage, as the loading displacement increased again, the oil pressure increased rapidly to 4.8 MPa until the secondary hydraulic fracture initiation occurred.

In the first stage, the loading displacement increased rapidly for 3 minutes, followed by a pause until 23 minutes (Fig. 7c), while the oil pressure remained at a low value with little change during this period. No fracture was initiated (Fig. 7d). In the second stage, the oil pressure increased rapidly from 23 to 35 minutes. The variation of the oil pressure curve in this interval period shows the first fracture initiation pressure of 6 MPa, followed by a second hydraulic fracture pressure of 6.7 MPa.

The displacement of sample C was maintained at a fixed growth rate (Fig. 7e). The initiation of the coal sample appeared at the beginning of the hydraulic fracturing from the variation on the oil pressure curve. The initiation pressure reached 7.0 MPa; the fracturing fluid expanded

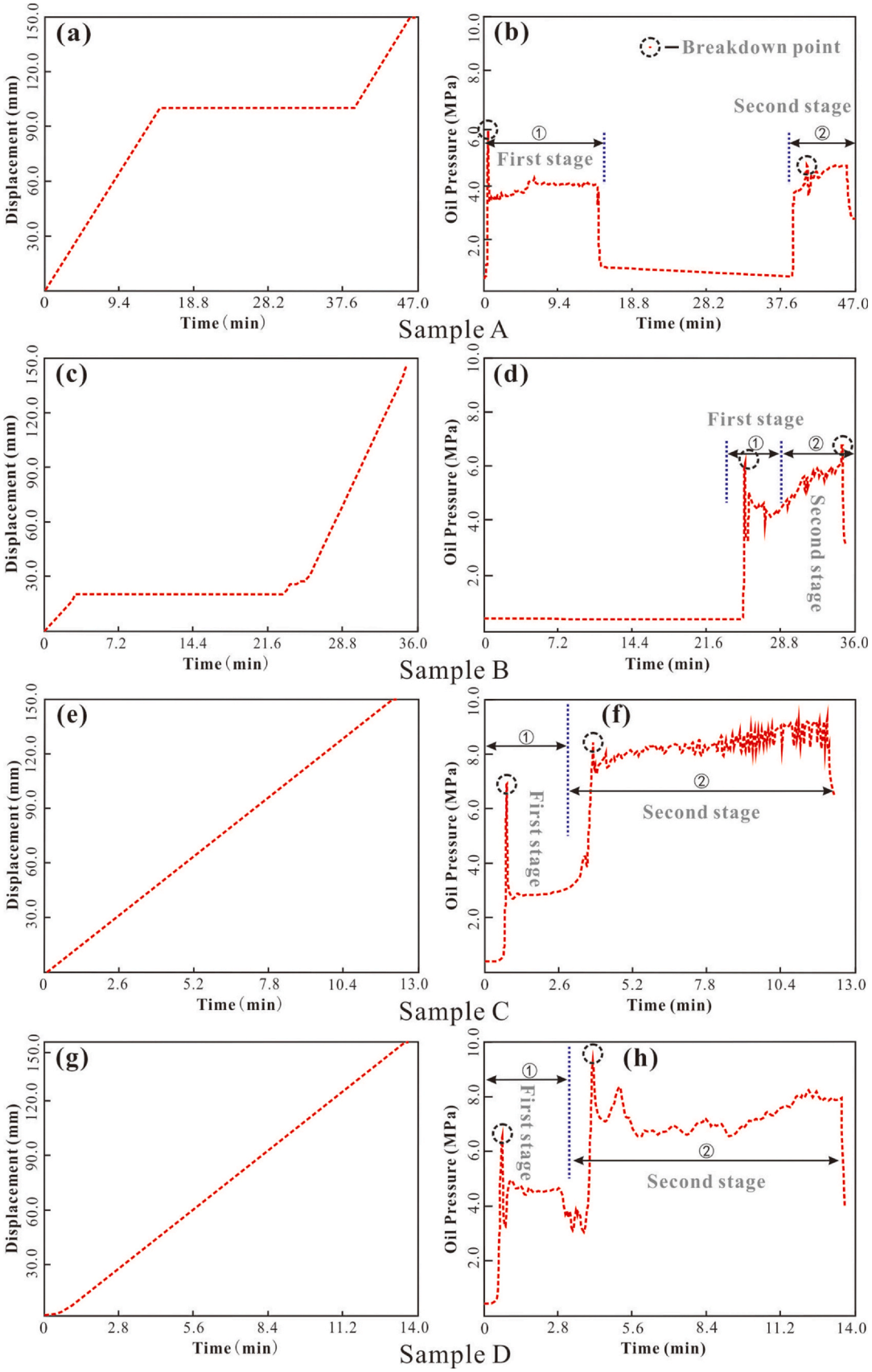

Fig. 7. (a), (c), (e), and (g) Depict the time-displacement curves during the fracturing process for samples A, B, C, and D, respectively. Note: The displacement refers to the scale at which the fracturing fluid is injected during the hydraulic fracturing process, which plays a crucial role in controlling the injection flow rate. Specifically, a faster injection speed corresponds to a higher injection rate. By adjusting the displacement, we can effectively manage and regulate the rate at which the fracturing fluid is injected into the sample. (b), (d), (f), and (h) Illustrate the time-oil pressure curves during fracturing for samples A, B, C, and D. The comprehensive fracturing procedure for each sample can be divided into two distinct stages.

along the fracture. The oil pressure decreased until the second fracture initiation with an initiation pressure of 8.4 MPa. The oil pressure fluctuated slightly within a specific range (Fig. 7 f). Considering the analysis results of the hydraulic fracturing fractures in sample C in Section 4.4.3, the fracturing fluid may break through the cement at around four minutes, resulting in a large amount of fracturing fluid leakage.

Like sample C, the loading displacement increased at a constant rate (Fig. 7 g). However, the injection flow rate was at 0.30 ml/s, only half that of sample C. The sample D was hydraulically broken down at about 1 minute, and the initiation pressure was 6.8 MPa. A second hydraulic rupture happened when the oil pressure increased rapidly in 4.5 minutes, with the fracture initiation pressure approximately 9.5 MPa (Fig. 7 h). Like in the case of sample C, both hydraulic rupture processes occurred twice. The oil pressure in sample D did not remain constant within a specific range after the second hydraulic rupture but continued to drop and then maintained at a particular field. The fracturing fluid leakage should have occurred after 5.5 minutes for the oil pressure to decrease rapidly from this point.

4.4. Hydraulic fracture initiation and propagation

4.4.1. Hydraulic fractures in sample A

The fractures on the sample's surface are all marked in white for better observation. As shown in Fig. 8, surface A-A (the first A is the sample number, then follows the surface number) is the horizontal plane to which the wellbore is perpendicular. A significantly large fracture formed on this surface, perpendicular to σ_H. The large fracture has a branch fracture at its mid-position, with its extension direction being approximately 30° to σ_H (Fig. 8a). However, the surface A-F, which is parallel to A-A, is not fractured as the base plate (Fig. 8f). The branching fracture formed on A-A extends vertically branching on surface A-B (Fig. 8b). No apparent fractures were found on the A-C surface, which is parallel to A-B (Fig. 8c). The vertical fractures formed on the surface A-A can be found both on A-D and A-E (Figs. 8d and 8e). A vertical fracture perpendicular to σ_H and another minor branching vertical fracture is mainly formed on the sample's surface.

Sample A was opened along the surface fracture. The white curves in Fig. 9 show the direction of propagation of the hydraulic fracture. Although the extension process has a slight offset, the general direction remains unchanged. Fig. 9a shows the primary hydraulic fractures, while Fig. 9b shows that the primary hydraulic fractures in the coal are roughly perpendicular to the direction of σ_H. Two vertical fractures formed (Fig. 9c), one of them next to the wellbore and the other one roughly parallel to the first vertical fracture. Fig. 9d shows that the fracturing fluids are found all around the wellbore, inducing large vertical fractures in the vertical direction. However, no significant volume of fracturing fluids was found along the bedding, which indicates that bedding planes do not behave as major fracturing fluid seepages under the current experimental conditions.

Fig. 10a shows no tracer near the wellbore. However, several minor fractures extending through bedding planes can be identified. Fig. 10b shows the opened sample, with some fracturing fluid leaching from the sample's surface. Figs. 10c, 10d, 10e, and 10f show the distribution of the fracturing fluid near the wellbore. The fracturing fluids and some minor fractures reveal that once a large fracture is formed near the wellbore, the fracturing fluids preferentially expand along the dominant fracture channel and are unlikely to cause re-fracturing, making it difficult for other large new fractures to form.

4.4.2. Hydraulic fractures in sample B

Bedding planes are oriented at approximately 30° to the wellbore direction in sample B. The vertical fracture formed on the B-A surface of the sample encasing cement is approximately parallel to the σ_h. In contrast, branching fractures are mostly obliquely to the direction of the σ_H at a slight angle (less than 45°) (Fig. 11a). Fractures on the B-B and B-C surfaces show a branching geometry and extend in the direction roughly parallel to σ_H (Figs. 11b and 11c). The fractures detected on the B-A surface do not develop too much in the vertical direction on the B-D and B-E surfaces (Figs. 11d and 11e). The surface B-F, which is parallel to the B-A, does not show fractures (Fig. 11f).

Sample B was also opened along the surface fracture. Similar to the fracture network observed on the surface, a series of minor parallel fractures formed in the vicinity of the wellbore, as shown by the white line in Fig. 12, with the strike direction parallel to the direction of σ_h (Fig. 12a). In contrast, two fractures formed in the direction diagonally intersecting the minor fractures, with the strike direction oriented approximately at 30° from the direction of σ_h. In addition, mutually vertical fractures also formed near the wellbore (Fig. 12b). When opening the sample along the surface B-B, the horizontal and vertical fractures can be found at the gap area between the coal sample and cement; they penetrate the cement and extend to the boundary. The vertical fracture in Fig. 12c corresponds to the branching fracture in Fig. 12a, indicating a certain correspondence between the fractures on the surface and the hydraulic fractures formed inside the coal sample.

4.4.3. Hydraulic fractures in sample C

The magnitude of the loaded horizontal stresses of sample C are 1.5 times higher than that of samples A and B, thus simulating complex structural extrusion conditions in the same coalbed methane reservoir. The vertical stress magnitude remained constant, i.e., the lateral pressure coefficient increased by 1.5 times, where $\sigma_H > \sigma_h > \sigma_v$. Irregular fractures formed on the C-A surface of the sample encasing cement, with no obvious preferred direction (Fig. 13a). The fractures on the C-B surface mainly appear along the σ_H direction (Fig. 13b). In contrast, the horizontal fractures parallel to the σ_h direction appear on the C-C surface (Fig. 13c). The vertical fractures parallel the σ_H direction are visible on the C-D and C-E surfaces. The inclined fractures intersecting the vertical direction also include the C-E surface. The fracture distribution with symmetry and variability indicates the high inhomogeneity of the coal sample (Figs. 13d and 13e). A large amount of fracturing fluid was found on the C-F surface, the base plate of the simulated coal reservoir, implying that the microfractures that formed served as the channel for the fracturing fluid filtration loss (Fig. 13f).

When opening sample C along its surface fractures, no obvious primary fractures could be seen in the upper part of the wellbore, and a few secondary fractures intersected diagonally with the σ_v direction (Figs. 14a and 14d). Fracturing fluids appear around the wellbore but without clear fractures (Figs. 14b and 14c). Figs. 14e and 14f show that no fractures were formed at the bottom of the wellbore, given that a large number of fracturing fluids leaching is found in Fig. 14f, which is why no primary fractures formed. While on the right side of the wellbore, a clear fracture propagation surface can be observed (Fig. 14e). As this configuration was intended to simulate the horizontal well fracturing, the wellbore was placed in the direction parallel to bedding in the coal sample, thus making the bedding planes the primary channels for fracturing fluid filtration loss.

4.4.4. Hydraulic fractures in sample D

The bedding orientation of sample D was perpendicular to the direction of the wellbore. A large amount of fracturing fluid filtration was found at the upper part of the wellbore. The primary fractures formed on the surface obliquely or parallel to the direction of σ_H (Fig. 15a), and secondary fractures were found on both the D-B and D-C surfaces, which are roughly parallel to the direction of σ_h. Moreover, some oblique fractures could be identified on the D-C surface (Figs. 15b and 15c). The fracture distribution on the D-D surface is

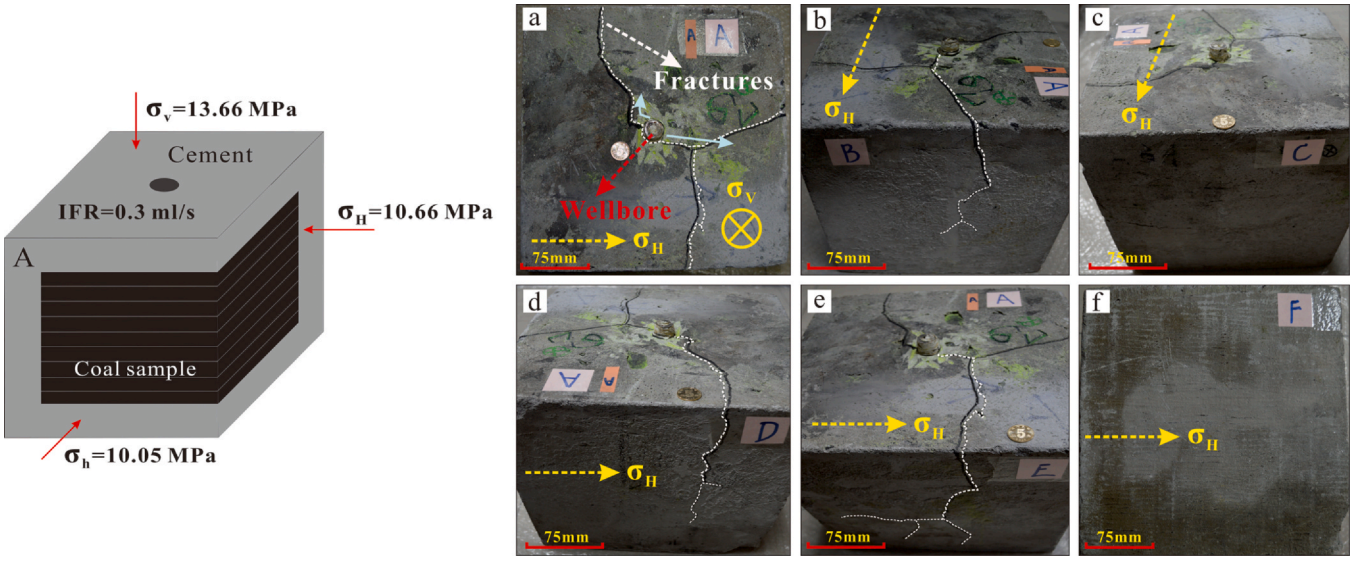

Fig. 8. Fracture distribution on the six surfaces of the cement bounding sample A (A-A, A-B, A-C, A-D, A-E, and A-F) after hydraulic fracturing of the sample. The yellow arrows denote the direction of the σ_H. (a) On the uppermost surface, designated as Surface A, the vertical stress (σ_v) operates perpendicular to the plane of the surface. The formation of two distinct fractures is evident, delineated by white dotted lines for clear visualization. (b) and (d) The vertical fractures are distinctly visible in the corresponding figures. (e) Beyond the vertical fracture, we can clearly observe the divergence of horizontal fractures at the midpoint of Surface E. (c) and (f) Upon examination of Surfaces C and F, there are no discernible fractures present.

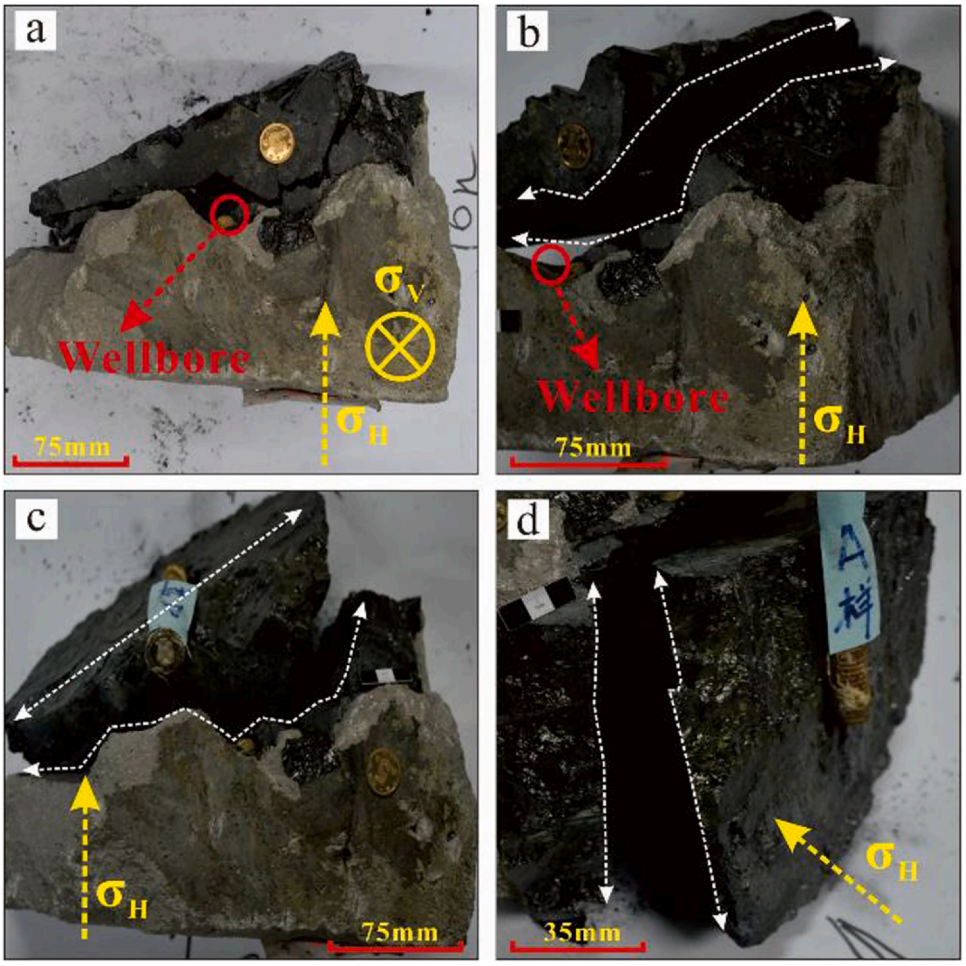

Fig. 9. Observation of the hydraulic fracture in sample A after fracturing. The yellow arrows denote the direction of the σ_H. (a) The occurrence of the primary hydraulic fracture; (b) The orientation or path of the primary hydraulic fracture; (c) The presence of two vertical fractures; (d) The distribution of fracturing fluids surrounding the wellbore.

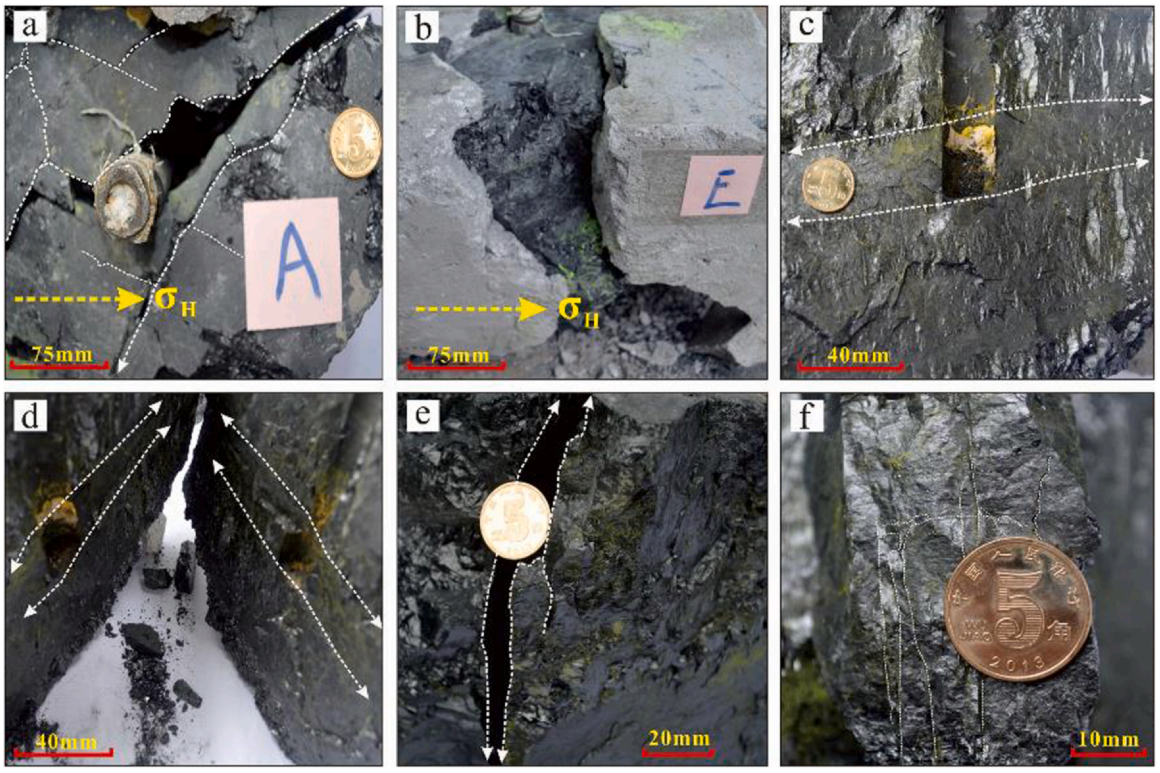

Fig. 10. Detailed observation of hydraulic fractures near the wellbore in sample A. The yellow arrows denote the direction of the σ_H. (a) Illustrates fractures in the vicinity of the wellbore; (b) Demonstrates fracturing fluid seeping from the surface; (c) and (d) Show typical flow paths of the fracturing fluid; (e) and (f) Represent the dispersal of the fracturing fluid around the wellbore area.

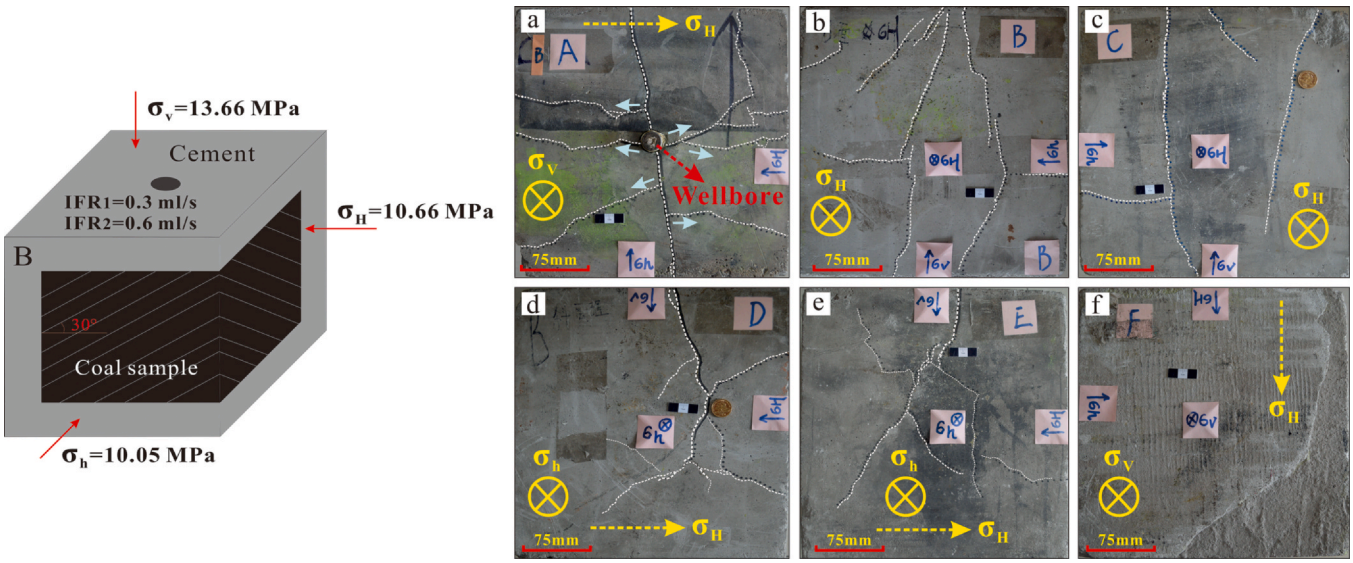

Fig. 11. Fracture distribution on the six surfaces of the sample encasing cement (B-A, B-B, B-C, B-D, B-E, and B-F) after hydraulic fracturing. The label papers and yellow arrows denote the direction of σ_H, σ_h, and σ_v. (a) Despite the presence of a significant fracture parallel to the σh direction, arrows near the wellbore designate all initial fracture propagation directions to be closely aligned with the σH direction; (b) and (c) Predominantly vertical and inclined fractures are observed, with few instances of horizontal fractures; (d) and (e) On these two mutually parallel surfaces, the formation of inclined fractures is the dominant feature; (f) This surface appears to be devoid of any observable fractures.

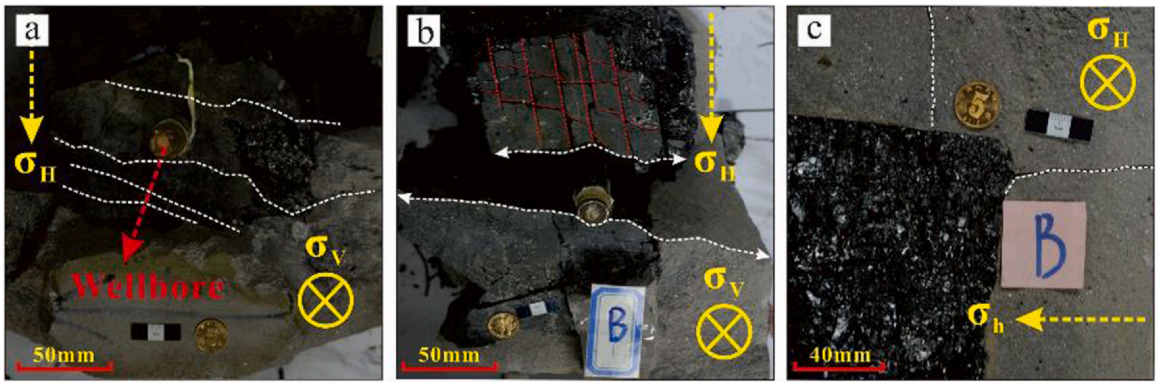

Fig. 12. Hydraulic fractures observed within Sample B. Yellow arrows represent the direction of the σ_H and the σ_h. (a) Illustrates fractures extending in a direction parallel to that of σ_h; (b) Showcases the emergence of vertical fractures closely situated to the wellbore. In addition, numerous natural fractures are observed near the wellbore. However, these fractures appear devoid of any fracturing fluids. (c) Depicts the coexistence of vertical and horizontal fractures.

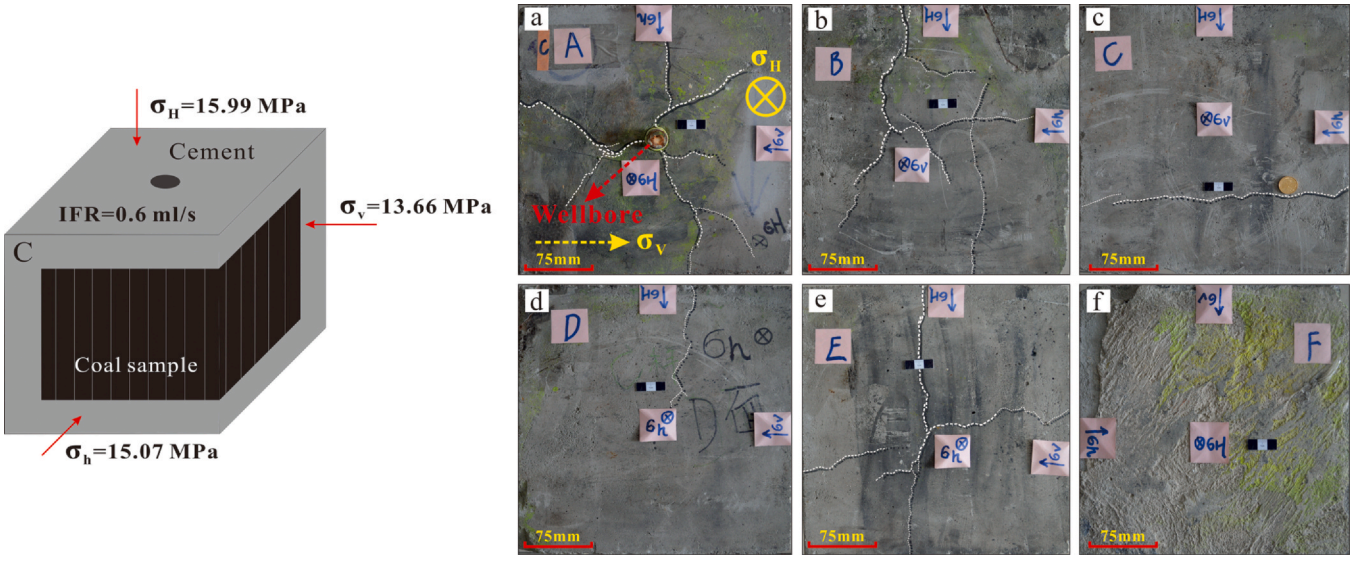

Fig. 13. Fracture distribution on the six surfaces of the sample encasing cement (C-A, C-B, C-C, C-D, C-E, and C-F) after hydraulic fracturing. The label papers and yellow arrow denote the direction of σ_H, σ_h, and σ_v. (a) A fracture system has formed without a clear directional pattern; (b) The dominant fractures are observed propagating along the σ_H direction; (c) Horizontal fractures run parallel to the σ_h direction; (d) Horizontal fractures are seen running parallel to the σ_H direction; (e) A mixture of horizontal and vertical fractures are present; (f) While this surface appears devoid of any discernible fractures, numerous leakages of fracturing fluid are noted.

more disordered, with some oblique fractures and some fracturing fluid found on this surface. No new fractures could be found on the D-E surface (Figs. 15d and 15e). A vertical fracture was visible on the D-F surface, and a large amount of fracturing fluid was found on this surface (Fig. 15f).

When sample D was opened along the surface fracture (Fig. 16a), a secondary fracture could be seen near the upper wellbore with the main direction parallel to that of σ_H (Fig. 16b), as well as a vertical fracture also roughly along the direction of σ_H (Fig. 16c). A large number of natural fractures developed at the upper left corner of the sample, and no fracturing fluid was leached from these natural fractures. Fig. 16d shows the irregular path of the vertical fracture extension. A series of horizontal bedding planes can be found on the D-B surface. However, no fracturing fluid was found (Fig. 16e). The main fracture form from this fracturing is hydraulically fractured and is not accompanied by the formation of the more minor secondary fractures (Fig. 16f).

5. Discussion

5.1. Impact of the injection flow rate and horizontal stress difference on hydraulic fracture

Although experiments D and C shared identical stress conditions, significant fracturing was observed in sample D despite the considerable fluid leakage observed during the experiment. This could be attributed to the lower injection flow rate applied to sample D (0.30 ml/s) versus the higher rate employed for sample C (0.60 ml/s). Notably, the oil pressure curves of the two experiments, run under similar stress and divergent injection flow rates, initially displayed a close resemblance, with significant distinctions emerging during the post-leakage stage (Fig. 7 f and 7 h). Despite both samples experiencing fracturing fluid leaks, sample C was able to sustain elevated oil pressure levels due to its higher injection flow rate. On the other hand, sample D, which had half the injection flow rate, exhibited a decline in oil pressure. These

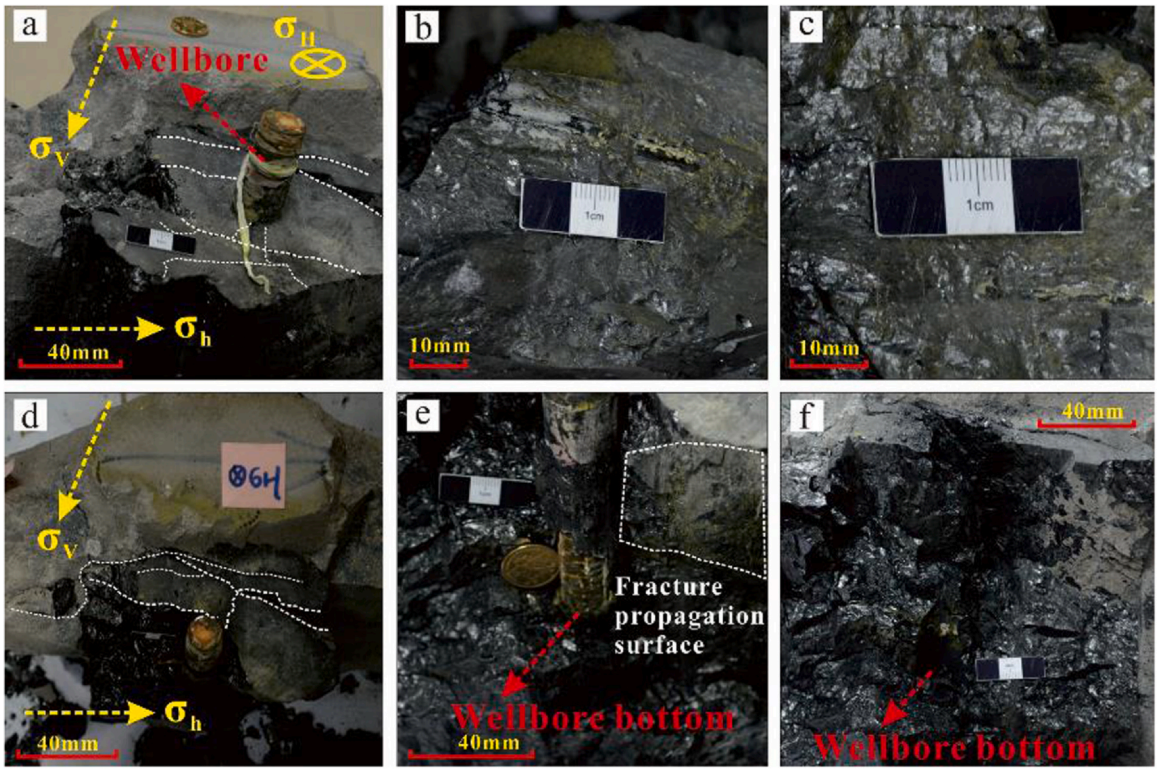

Fig. 14. Detailed observation of hydraulic fractures in sample C. The yellow arrows denote the direction of σ_H, σ_h, and σ_v. (a) and (d) Several secondary fractures are observed intersecting the σ_v direction diagonally; (b) and (c) Fracturing fluids are noticeable in the area surrounding the wellbore; (e) No fractures have formed near the wellbore, although a fracture surface has emerged on the right side of the wellbore; (f) Leakage of fracturing fluids is observed.

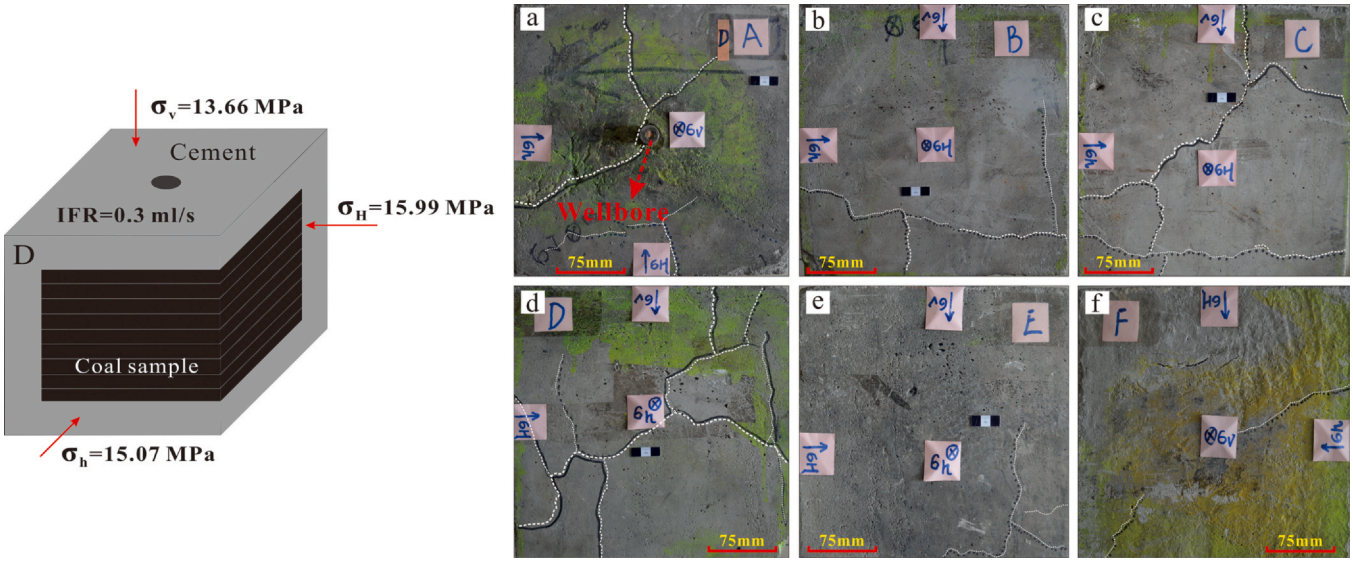

Fig. 15. Fracture distribution on the six surfaces of the sample encasing cement (D-A, D-B, D-C, D-D, D-E, and D-F) after hydraulic fracturing. The label papers mark the direction of σ_H, σ_h, and σ_v. (a) The fracture system primarily aligns with the σ_H direction; (b) Both horizontal and vertical fractures are present; (c) and (d) In both cases, their fracture systems have developed without a discernible directional pattern; (e) Several secondary fractures have materialized in the corner of Surface E; (f) A fracture is evident on the bottom surface, leakage of fracturing fluids have been observed.

observations indicate that high injection flow rates can uphold substantial pressures within the fractures, even amidst fracturing fluid leakages associated with the initial high injection flow rates, and consequently facilitate the continued opening and propagation of hydraulic fractures. Similar findings have been confirmed by Zhang et al. (2022). that with an increase in fracture geometry, there is a corresponding rise in the critical propagation volume required for each step. On the contrary, low injection flow rates make difficult to fracture the reservoir and impedes the creation of new fractures following a fracturing fluid leak. This condition underscores the crucial role of an optimal injection

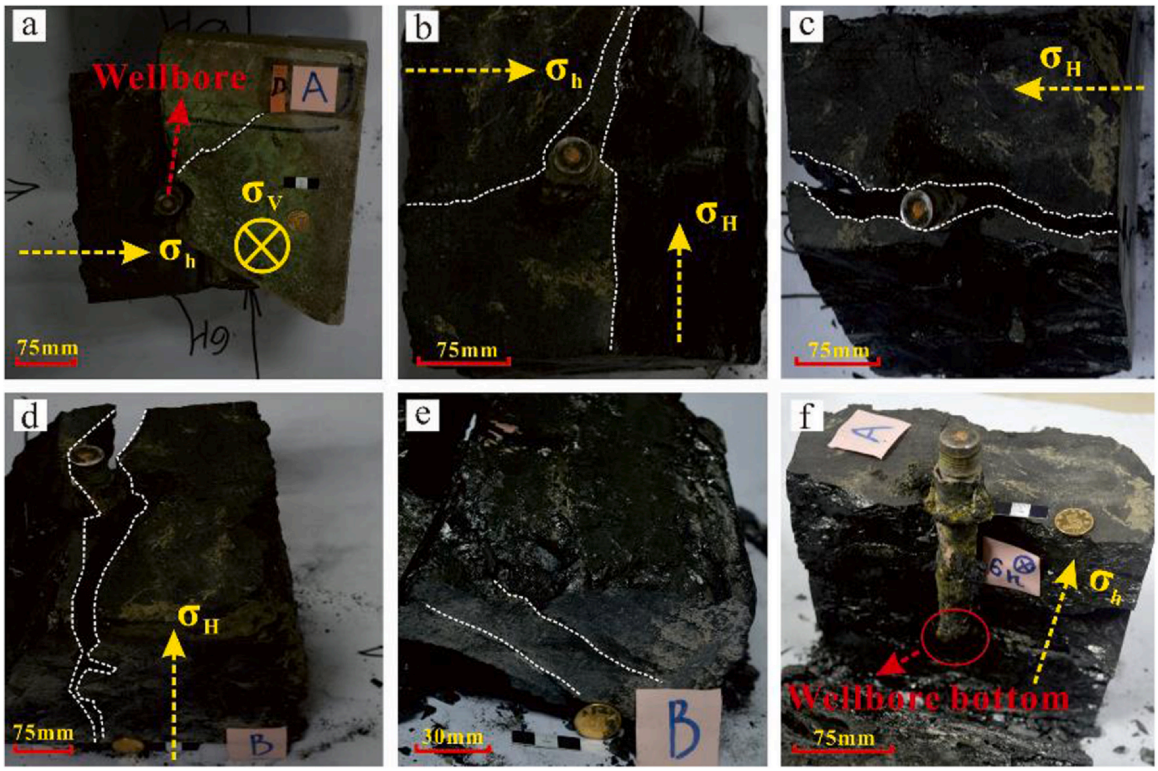

Fig. 16. Detailed observation of hydraulic fractures in sample D. The yellow arrows denote the direction of σ_H, σ_h, and σ_v. (a) The sample is dissected along the fracture lines; (b) A secondary fracture is evident, with its primary direction parallel to that of σ_H; (c) A main vertical fracture is roughly aligned with the σ_H direction; (d) The primary fracture extension follows an irregular trajectory; (e) There is no observable leakage of fracturing fluids; (f) No additional minor secondary fractures are being formed.

rate in maintaining the efficiency of hydraulic fracturing processes. The experimental study by Jiang et al. (2023). demonstrated that at low injection rate, fractures steadily propagate at a slow velocity, creating numerous parallel fractures along the joints; conversely, a high injection rate results in swift fracture propagation, culminating in a single primary fracture. However, for settings with a low injection rate might be insufficient to initiate fracturing in the coal reservoir. For instance, sample B did not initially fracture at an injection rate of 0.3 ml/s and only commenced fracturing when the rate was increased to 0.6 ml/s, as shown in Figs. 7c and 7d. Our experimental results indicate that higher injection rates lead to enhanced fracturing efficiency. However, it is crucial to minimize roof and floor fracturing in coal reservoirs to prevent fracturing fluid leakage, thus ensuring fracturing efficiency.

The horizontal stresses in sample D were imposed to be 1.5 times that of sample A, engendering an amplification of the lateral pressure coefficient. This stress variance induced a shift in the directional propagation of the principal hydraulic fractures across the two samples. Under the prescribed horizontal stresses, σ_H and σ_h, at 10.66 MPa and 10.05 MPa respectively, the dominant hydraulic fracture in sample A propagated in a direction closely aligned with σ_h (Fig. 18a). However, an increase in the horizontal stresses to 15.99 MPa and 15.07 MPa induced a pronounced stress difference, causing the primary hydraulic fracture in sample D to propagate along the σ_H direction (Fig. 18b). While Laubach et al. (2004). proposed that open natural fractures may not necessarily align with the σ_H, our study underscores that significant differences in horizontal stress primarily steer hydraulic fracture propagation along the σ_H axis. This insight can serve as a foundational reference for predicting the directionality of hydraulic fracture propagation. An alternate perspective proposes that fractures could penetrate the coal-rock interface (similar to the coal roof and floor in our study) when the differential stress is greater than or equal to 7.0 MPa; however, when the stress difference falls below 7.0 MPa, fractures tend to expand along the coal-rock interface without successfully penetrating it (Jiang et al., 2023). Sherratt et al. (2023) concurred that a low differential stress, even as low as 4 MPa, enhances the tendency of hydraulic fractures to propagate along weak planes, and moreover, proposed that adjusting the well orientation not parallel to the direction of minimum horizontal stress could further improve recovery. Accordingly, the hydraulic fracture exploits beddings in the experiment may be the reason why the dominant hydraulic fracture in sample A propagated not along the σ_H but closely aligned with σ_h (Fig. 18a). Given the real in-situ stress conditions of the targeted coal reservoir, we did not set such a substantial horizontal stress difference, however, our experimental results displayed fractures in the coal roof of both samples A and D. Additionally, the initiation pressure in sample A (6.0 MPa and 4.8 MPa) was significantly lower than in sample D (6.8 MPa and 9.5 MPa), indicating that reservoirs with higher lateral pressure coefficients, thus, elevated horizontal stress, demanding greater hydraulic pressures to facilitate the formation of new fractures.

5.2. *Effect of bedding orientation on hydraulic fracturing*

The orientation of bedding planes significantly influences the coal structure, thereby playing a crucial role during hydraulic fracturing (Li, 2001). Experimental and numerical simulations by Wang et al (Wang et al., 2021c). demonstrated that the bedding plane orientation strongly influences the direction of fracture propagation in coal specimens and can also result in the transition of crack mode. When bedding plane

Fig. 17. (a) and (d) Depict the fracture systems on the top surface, simulating the coal roof, of samples A and D, both subjected to a constant injection flow rate of 0.3 ml/s; (b) and (c) Show the fracture systems of samples B and C, exposed to injection flow rates of 0.3–0.6 ml/s and a consistent 0.6 ml/s, respectively. Dashed lines of varying widths and colors denote fractures of different scales: primary fractures, secondary fractures, and minor fractures.

angles are equal to or less than 45.0° respect to the horizontal stresses, the pure mode I crack transitions into a mixed-mode I-II after fracture initiation. On the other hand, when the angles exceed 45.0°, the crack mode remains predominantly mode I throughout the propagation process, indicating that the bedding plane has minimal influence on the crack behavior. Further studies indicate that the propagation path of hydraulic fractures can be influenced by both the orientation of the bedding plane and the orientation of the maximum principal stress (He and Duan, 2019; Fan et al., 2014; Huang and Liu, 2017; Huang et al., 2023). In our research, bedding orientations were set to 0° and 30° relative to the horizontal plane in samples A and B, respectively. This has resulted in the formation of a complex network of hydraulic fractures in sample B, exhibiting numerous fractures approximately parallel to σ_H, and several minor fractures parallel to σ_h (Figs. 9 and 12). Moreover, several intersecting fractures led to a notable improvement in hydraulic fracturing efficiency and significantly enhanced reservoir permeability. Contrary to Huang et al (Huang et al., 2023). 's observation that the bedding angle has a minimal impact on the initial fracture pressure during the hydraulic fracturing process in coal, our results indicate that sample B underwent higher initiation pressures (6.3 MPa and 6.7 MPa) compared to those of Sample A (6.0 MPa and 4.8 MPa). Accordingly, these findings suggest that even a slight deviation in the angle between the injection direction of the wellbore and bedding orientation can result in the formation of a complex network of hydraulic fractures.

5.3. Hydraulic fracturing pressure during re-fracturing

The experimental study of Wei et al. (2020) shows that the initiation pressure tends to be higher if the initiation time period is shorter. As depicted in Fig. 19a, our experimental results also draw a similar trend. This suggests that, as the initiation time increases, it takes more time for the fracturing fluid to flow through natural fractures or bedding planes. This results in energy consumption, leading to a lower fluid pressure required to initiation hydrofracturing. Fig. 19b further reveals that the initiation pressures from our experiments predominantly ranged

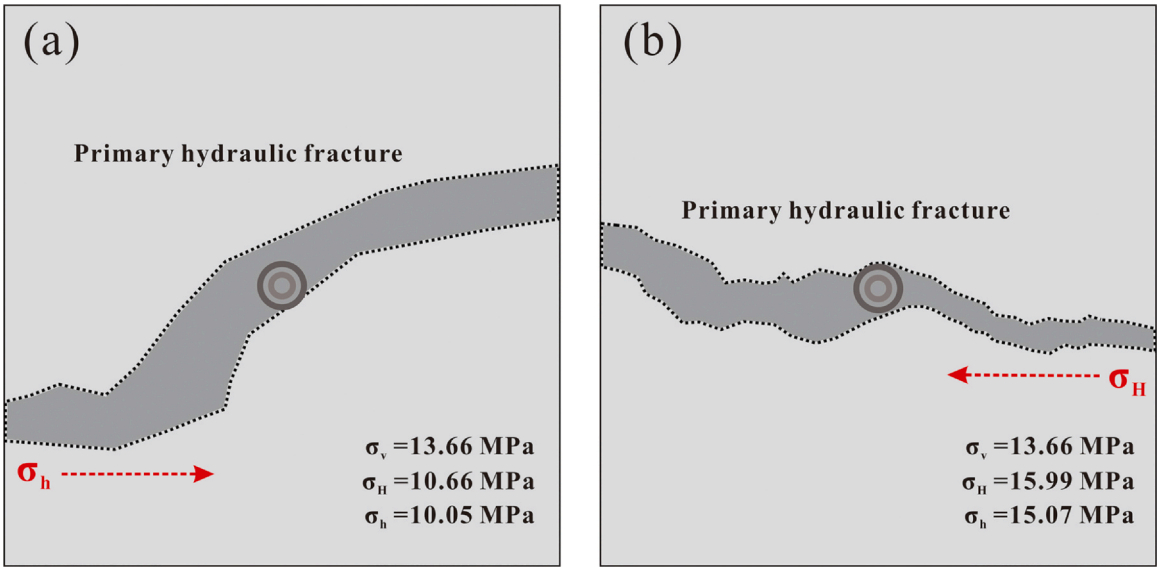

Fig. 18. (a) and (b) Sketch of the primary hydraulic fractures within the coal block of samples A and D under their respective differing confining stress conditions.

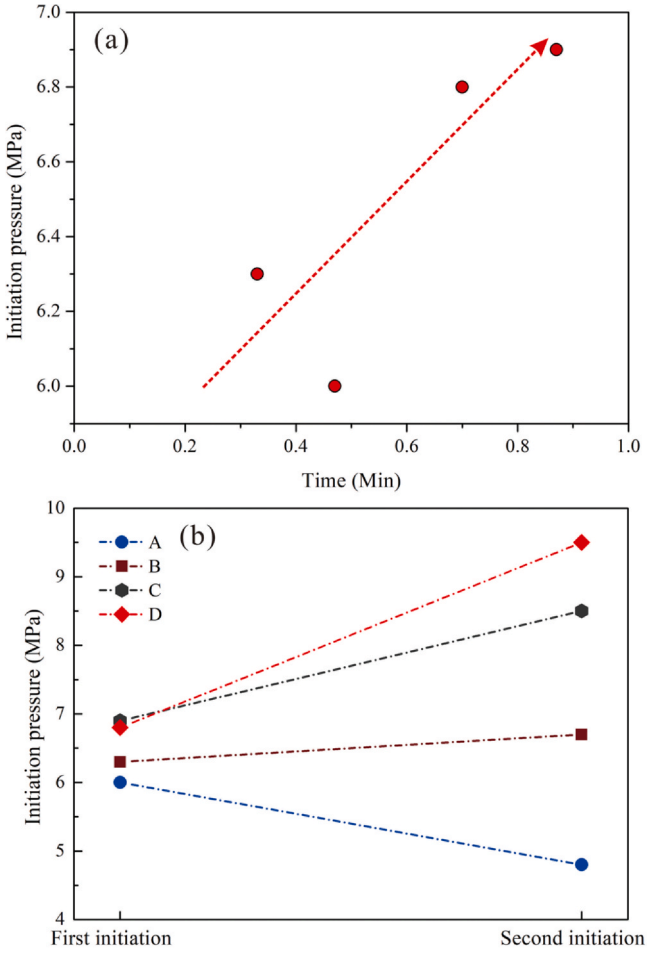

Fig. 19. (a) First initiation pressure and corresponding time, with trend indicated by red arrow. Note: the initiation time represents the duration between the onset of the rapid increase in oil pressure and the subsequent rapid decrease. It serves as a measure of the time during which the fracture initiation and propagation occur. (b) Comparative analysis of initial and subsequent initiation pressures in re-fracturing.

Table 7
Breakdown pressure of experimental test and analytical solutions.

Sample No.	σ_H (MPa)	σ_h (MPa)	Breakdown pressure (MPa)		
			H-W solution	H-F solution	Experimental
A	10.66	10.05	20.99	18.68	6.00
B	10.66	10.05	20.99	18.68	6.30
C	15.99	15.07	30.72	26.09	6.90
D	15.99	15.07	30.72	26.09	6.80

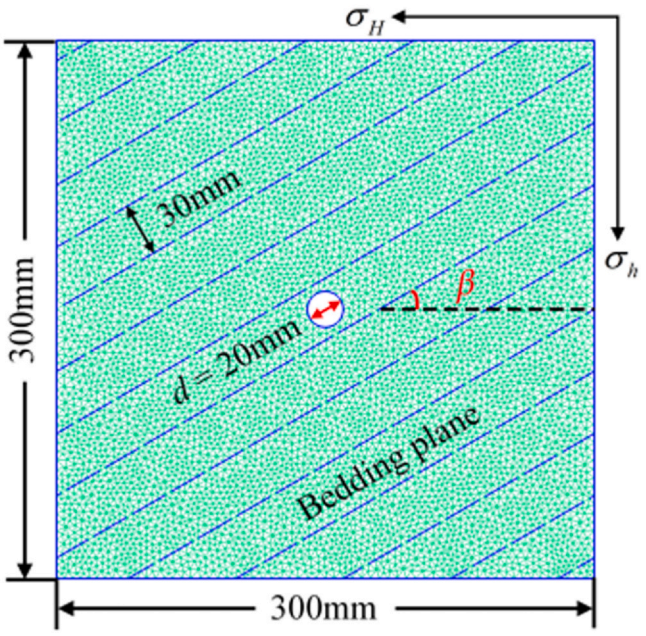

Fig. 20. Schematic diagram of a two-dimensional model. See main text for definition of parameters.

Table 8
Parameter settings for the numerical model.

	Parameter	Value	Unit
Rock matrix	Young's modulus, E	3.72	GPa
	Poisson's ratio, μ	0.32	-
	Bulk density, ρ	1505	kg/m^3
	Cohesion, c_0	9.98	MPa
	Friction angle, $\varnothing_0$	35.73	(°)
	Tensile strength, σ_{t0}	1.5	MPa
	Permeability, k	9×10^{-17}	m^2
	Porosity, ε	0.08	-
	Biot coefficient	0.665	-
	Initial aperture, a_0	1×10^{-7}	m
	Minimum aperture, a_{min}	1×10^{-7}	m
	Maximum aperture, a_{max}	4×10^{-5}	m
Bedding plane	Cohesion, c_1	7	MPa
	Friction angle, $\varnothing_1$	32	(°)
	Tensile strength, σ_{t1}	1.1	MPa
	Initial aperture, a_{01}	2×10^{-6}	m
	Minimum aperture, a_{min1}	2×10^{-6}	m
	Maximum aperture, a_{max1}	4×10^{-5}	m
Fluid	Injection rate, q	0.3	ml/s
	Fluid viscosity, v	0.001	Pa·s
	Bulk modulus, K_w	2.2	GPa
Stress condition	Horizontal maximum principal stress, σ_H	10.66	MPa
	Horizontal minimum principal stress, σ_h	10.02	MPa

between 6.0 MPa and 7.0 MPa, revealing that the samples derived from identical coal mines, exhibited relatively similar mechanical characteristics. Despite identical stress conditions and injection flow rates, the results show that bedding orientation about the wellbore significantly influenced initiation pressure in samples A and B. The recorded initiation pressures for samples A and B were noticeably lower than those of samples C and D, suggesting that higher horizontal stress contributes to an elevated initiation pressure. Additionally, subsequent initiation pressures for samples B, C, and D markedly exceeded their preceding values, implying that multiple hydraulic fracturing requires additional increments in hydraulic pressure.

Additionally, it is meaningful that theoretically calculated values can be used to compare with experimental or simulation data (Mollaali et al., 2019). Therefore, the breakdown pressure (initiation pressure) values were compared with the linear elastic Hubbert-Willis (H–W) solution, (Hubbert and Willis, 1972) and the poroelastic Haimson-Fairhurst (H–F) solution (Haimson and Fairhurst, 1967). For the calculation, we assumed an average tensile strength of 1.5 MPa (from Table 2), an average Biot coefficient of 0.665 (from Table 4), a Poisson's ratio (μ) of 0.32 derived from the averaged values obtained in the No. 3 coal seam in the Zhengzhuang area, and an average pore pressure (Po) of 3.54 MPa (Huang et al., 2019). The breakdown pressures from these diverse solutions are presented in Table 7. The breakdown pressure values from the H-W solution are consistently higher than those from the H-F solution. Despite the variability in breakdown pressures obtained in in-situ tests in the No. 3 coal seam in the Zhengzhuang area (ranging from 11.07 MPa to 31.38 MPa, as reported by Huang et al (Huang et al., 2019)), all of them surpass the values obtained from the experimental solution. Although pressure correction was used with the stress transfer simulations, the use of a concrete ring to protect the sample or the large size of the experimental samples, it is challenging to fully replicate the in-situ reservoir conditions under laboratory conditions, and the experimental results also have limitations. However, laboratory experiments still contribute to a deeper understanding of the propagation patterns of hydraulic fracturing fractures.

5.4. A simplified numerical simulation verifying

Building upon the findings of our hydraulic fracturing experiments, the role of bedding orientation to the main principal stresses was not conclusive. Therefore, we performed a streamlined numerical simulation to ascertain its potential influence on fracture propagation and network geometry. Leveraging Multi FracS, a widely employed software for multi-physics fracture analysis, (Wang et al., 2024; Yan et al., 2023a, 2023b) our simulation prioritized result-focused implementation, serving as validation for our experimental outcomes.

In Fig. 20, we illustrate a two-dimensional coal model featuring multiple bedding interfaces. The model dimensions are 300 mm × 300 mm, with a 20 mm diameter water injection area. Bedding is represented by discontinuous joints, spaced at 30 mm intervals, with the angle β denoting the inclination of bedding planes relative to σ_H. We consider β values of 0°, 30°, and 90°, similar to our experiments. Additionally, all model sides have fixed normal displacement boundaries. The model is subjected to both σ_H and σ_h forces. The Delaunay algorithm is employed for mesh generation. This algorithm is capable of attaining a good fracture propagation effect during the simulation of hydraulic fracturing via the finite discrete element method (FDEM). It effectively controls triangle quality, precluding the formation of ill-shaped triangles and enhancing numerical accuracy and stability. The empty circumcircle property ensures uniform mesh distribution, minimizing errors from density variation. With robust adaptability to complex geometries, it precisely discretizes regions with irregular boundaries and internal holes, constructing a high-quality mesh framework for the numerical model and guaranteeing the reliability and precision of the simulation.

The material parameters were defined according to the rock matrix properties (E, μ, ρ, Biot coefficient, etc.), bedding plane characteristics (c_1, $\varnothing_1$ and σ_{t1}) and, fluid properties (q, v, K_w). Values for c_0, $\varnothing_0$, k, and ε are derived from averaged values obtained during rock mechanics tests. The aperture parameters for both the rock matrix and bedding planes are determined through trial-and-error method, while the mechanical properties of the bedding planes are adjusted to reflect a specific weakening effect compared to those of the rock matrix, as summarized in Table 8.

Stress conditions (σ_H and σ_h) and fluid injection rate are similar to those used during A and B experiments. In Fig. 21, we observe the morphology of fracture propagation across varying bedding angles (β = 0°, 30°, and 90°). The numerical simulations reveal distinct patterns: at β = 0° and 90°, three initiation points emerge in the coal model due to a low horizontal differential stress (0.64 MPa), prompting hydraulic fractures to spread indiscriminately towards the model periphery. Intersecting bedding interfaces provoke continuous branching and deviation of hydraulic fractures, leading to a complex network within the coal. Conversely, at β = 30°, the model displays only two initiation points. Hydraulic fractures experience pronounced shear displacement along bedding planes, resulting in simplified patterns primarily aligned with σ_H. In summary, the presence of weak bedding planes promotes intricate fracture networks. Despite numerical simulations forming primarily a single main fracture at β = 30°, largely aligned with σ_H, experimental results exhibit numerous fractures approximately parallel to σ_H.

The simulation reveals that the highest injection pressures for β = 0°, 30°, and 90° are 19.5 MPa, 18.6 MPa, and 19.8 MPa, respectively. Those fluid pressures are more coherent with breakdown pressures expected from the analytical solutions (Table 7) or observed during in-situ hydraulic tests in the coal reservoir. Notably, conditions at β = 0° and 90° result in a more intricate hydraulic fracture network at higher injection pressures. Conversely, achieving a simplified fracture pattern at lower injection pressures is more feasible at β = 30°, for

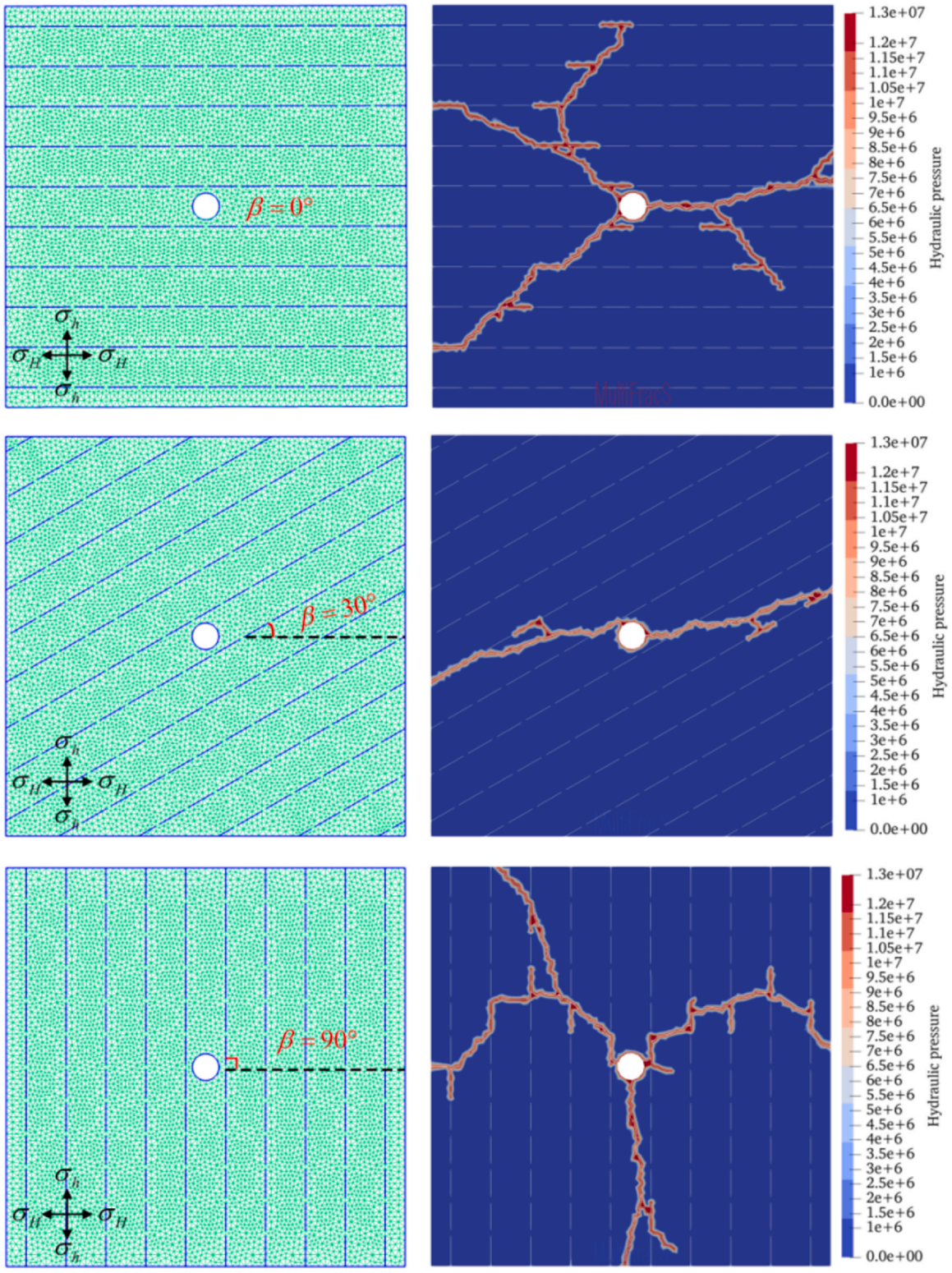

Fig. 21. Initial setup and hydraulic pressure pattern for the hydraulic fracturing models in coal. The fracture propagation morphology for different bedding angles (beta).

orientation with moderate shear stress. These findings suggest that deliberately orienting fractures to intersect bedding planes at low or high angles during hydraulic fracturing enhances the formation of fracture networks and, significantly, improves hydraulic fracturing efficiency.

6. Conclusions

This study investigates the fracture initiation and propagation behavior of anthracite using a true-triaxial hydraulic fracturing apparatus. The effects of injection flow rate, horizontal stress difference, and

bedding orientation on the effectiveness of hydraulic fracturing are examined. The main findings from this experimental research are summarized below:

(1) Initiating hydraulic fracturing with a high injection flow rate tends to result in fracturing fluid leakage. Nonetheless, a high injection flow rate also has the effect of sustaining significant pressures within the fractures, thereby fostering the sustained expansion and propagation of these hydraulic fractures. Enhanced fracturing efficiency can be achieved through higher injection rates, emphasizing the importance of minimizing roof and floor fracturing in coal reservoirs to prevent fracturing fluid leakage.
(2) A high horizontal stress difference tends to cause hydraulic fractures to propagate along the σ_H direction, although this may not always be the case at a lower horizontal stress difference. Furthermore, a high horizontal stress difference requires higher hydraulic pressure to create a new fracture system in coal reservoirs.
(3) A slight deviation in the wellbore injection direction from the bedding orientation promotes the creation of a complex hydraulic fracturing network, although this requires higher hydraulic pressure to initiate new fractures.
(4) During multiple hydraulic fracturing, the second initiation pressure is typically higher than the first one, implying that sequentially escalating the hydraulic pressure in multiple hydraulic fracturing aids in the generation of additional hydraulic fractures.

CRediT authorship contribution statement

Mengyao Wang: Software. **Yin Xing:** Data curation. **Yang Zhao:** Data curation. **Saipeng Huang:** Writing – original draft, Visualization, Resources, Methodology, Investigation, Funding acquisition, Data curation. **Dameng Liu:** Supervision, Project administration, Funding acquisition. **Enrique Gomez-Rivas:** Writing – review & editing, Methodology. **Albert Griera:** Writing – review & editing, Methodology. **Quan Gan:** Methodology.

Data availability

The data that has been used is confidential.

Declaration of Competing Interest

The authors declare that they have no known competing financial interests or personal relationships that could have appeared to influence the work reported in this paper.

Acknowledgements

The research work is funded by the National Natural Science Foundation of China (No.42202155), China Postdoctoral Science Foundation (No.2021MD703807), Heilongjiang Provincial Postdoctoral Science Foundation (No.LBH-Z20121). The authors also gratefully acknowledge financial support from the China Scholarship Council (No.202008230018) and the Research Fund Program of Hubei Key Laboratory of Resources and Eco-Environment Geology (No.HBREGKFJJ-202309). SH and EGR acknowledge funding by the DGICYT Spanish Project (grant no. PID2020–118999GB-I00), funded by the MCIN/AEI/10.13039/501100011033. EGR acknowledges funding by the Ramón y Cajal fellowship (grant no. RyC-2018–026335-I), funded by the MCIN/AEI/10.13039/501100011033 and the European Social Fund - Investing in Your Future.

References

Bohloli, B., Pater, C.J.D., 2006. Experimental study on hydraulic fracturing of soft rocks: influence of fluid rheology and confining stress. J. Pet. Technol. 53, 1–12.
Bons, P., Cao, D., De Riese, T., González-Esvertit, E., Koehn, D., Naaman, I., Sachau, T., Tian, H., Gomez-Rivas, E., 2022. A review of natural hydrofractures in rocks. Geol. Mag. 159 (11 − 12), 1952–1977.
Bredehoeft, J.D., Wolff, R.G., Keys, W.S., Shuter, E., 1976. Hydraulic fracturing to determine the regional in situ stress field, Piceance Basin, Colorado. Geol. Soc. Am. Bull. 87, 250–258.
Cai, Y.D., Liu, D.M., Yao, Y.B., Li, J.Q., Qiu, Y.K., 2011. Geological controls on prediction of coalbed methane of No. 3 coal seam in Southern Qinshui Basin, North China. Int J. Coal Geol. 88, 101–112.
Chen, M.J., Sun, Y.W., Fu, P.C., Carrigan, C.R., Lu, Z.M., Tong, C.H., Buscheck, T.A., 2013. Surrogate-based optimization of hydraulic fracturing in pre-existing fracture networks. Comput. Geosci. -UK 58, 69–79.
Chen, S.D., Tang, D.Z., Tao, S., Xu, H., Li, S., Zhao, J.L., Cui, Y., Li, Z., 2018. Characteristics of *in-situ* stress distribution and its significance on the coalbed methane (CBM) development in Fanzhuang-Zhengzhuang block, Southern Qinshui Basin, China. J. Pet. Sci. Eng. 161, 108–120.
Fan, T., Zhang, G., Cui, J., 2014. The impact of cleats on hydraulic fracture initiation and propagation in coal seams. Pet. Sci. 11, 532–539.
Gomez-Rivas, E., Griera, A., 2012. Shear fractures in anisotropic ductile materials: an experimental approach. J. Struct. Geol. 34, 61–76.
Grasselli, G., Lisjak, A., Mahabadi, O.K., Tatone, B.S.A., 2015. Influence of pre-existing discontinuities and bedding planes on hydraulic fracturing initiation. Eur. J. Environ. Civ. En. 19, 580–597.
Guo, T.K., Zhang, S.C., Qu, Z.Q., Zhou, T., Xiao, Y.S., Gao, J., 2014. Experimental study of hydraulic fracturing for shale by stimulated reservoir volume. Fuel 128, 373–380.
Haimson, B., Fairhurst, C., 1967. Initiation and extension of hydraulic fractures in rocks. Soc. Pet. Eng. J. 7 (3), 310–318.
Haimson, B.C., Cornet, F.H., 2003. ISRM Suggested Methods for rock stress estimation—Part 3: hydraulic fracturing (HF) and/or hydraulic testing of pre-existing fractures (HTPF). Int J. Rock. Mech. Min. Sci. 40, 1011–1020.
He, Z.H., Duan, B.C., 2019. Dynamic modeling of bedding-plane slip during hydraulic fracturing. Geophysics 84, 1–42.
Hu, Q.T., Liu, L., Li, Q.G., Wu, Y.Q., Wang, X.G., Jiang, Z.Z., Yan, F.Z., Xu, Y.C., Wu, X.B., 2020. Experimental investigation on crack competitive extension during hydraulic fracturing in coal measures strata. Fuel 265, 117003.
Huang, B., Liu, J., 2017. Experimental investigation of the effect of bedding planes on hydraulic fracturing under true triaxial stress. Rock. Mech. Rock. Eng. 50, 2627–2643.
Huang, L.S., Li, B., Wang, B., Zhang, J.X., 2023. Effects of coal bedding dip angle on hydraulic fracturing crack propagation. Geomech. Geophys Geo-Energ. Geo-Resour. 9, 30.
Huang, S.P., Liu, D.M., Yao, Y.B., Gan, Q., Cai, Y.D., Xu, L.L., 2017. Natural fractures initiation and fracture type prediction in coal reservoir under different *in-situ* stresses during hydraulic fracturing. J. Nat. Gas. Sci. Eng. 43, 69–80.
Huang, S.P., Liu, D.M., Cai, Y.D., Gan, Q., 2019. *In situ* stress distribution and its impact on CBM reservoir properties in the Zhengzhuang area, southern Qinshui Basin, North China. J. Nat. Gas. Sci. Eng. 61, 83–96.
Hubbert, M.K., Willis, D.G., 1972. Mechanics of Hydraulic Fracturing. AAPG Special Volumes.
Iqbal, O., Ahmad, M., Kadir, A., 2018. Effective evaluation of shale gas reservoirs by means of an integrated approach to petrophysics and geomechanics for the optimization of hydraulic fracturing: a case study of the Permian Roseneath and Murteree Shale Gas reservoirs, Cooper Basin, Australia. J. Nat. Gas. Sci. Eng. 58, 34–58.
Jiang, Y.L., Liang, W.G., Cai, T.T., Zhang, X.Q., Yan, J.B., Yue, S.F., 2023. Fracture growth and acoustic emission response in natural coal-rock blocks with different stress, fracturing medium and injection rates. J. Pet. Sci. Eng. 220 (part A), 111228.
Ju, W., Jiang, B., Miao, Q., Wang, J.L., Qu, Z.H., Li, M., 2018. Variation of in situ stress regime in coal reservoirs, eastern Yunnan region, South China: implications for coalbed methane production. AAPG Bull. 102, 2283–2303.
Kaiser, J., 1953. Erkenntnisse und Folgerungen aus der Messung von Geräuschen bei Zugbeanspruchung von metallischen Werkstoffen. Arch. Fr. Das. Eisenhttenwes 24, 43–45.
Laubach, S.E., Olson, J.E., Gale, J.F.W., 2004. Are open fractures necessarily aligned with maximum horizontal stress? Earth Planet Sc. Lett. 222, 191–195.
Lehtonen, A., Cosgrove, J.W., Hudson, J.A., Johansson, E., 2012. An examination of in situ rock stress estimation using the Kaiser effect. Eng. Geol. 124, 24–37.
Li, C.C., Liu, D.M., Cai, Y.D., Yao, Y.B., 2016. Fracture permeability evaluation of a coal reservoir using geophysical logging: a case study in the Zhengzhuang area, Southern Qinshui Basin. Energy Explor Exploit 34, 378–399.
Li, D.Q., Zhang, S.C., Zhang, S.A., 2014. Experimental and numerical simulation study on fracturing through interlayer to coal seam. J. Nat. Gas. Sci. Eng. 21, 386–396.
Li, H.Y., 2001. Major and minor structural features of a bedding shear zone along a coal seam and related gas outburst, Pingdingshan coalfield, northern China. Int J. Coal Geol. 47, 101–113.
Lin, R., Ren, L., Zhao, J.Z., Wu, L.Z., Li, Y.Z., 2017. Cluster spacing optimization of multi-stage fracturing in horizontal shale gas wells based on stimulated reservoir volume evaluation. Arab J. Geosci. 10, 38.
Liu, H.B., Jiang, B., He, W.Y., 2021. Characteristics of the in situ stress field in the Yadian Coal Mine, central China: implications for roadway differential deformation. ACS Omega 6, 739–746.
Liu, J., Yao, Y.B., Liu, D.M., Xu, L.L., Elsworth, D., Huang, S.P., Luo, W.J., 2018. Experimental simulation of the hydraulic fracture propagation in an anthracite coal reservoir in the southern Qinshui basin, China. J. Pet. Sci. Eng. 168, 400–408.
Liu, Z., Chen, M., Zhang, G., 2014. Analysis of the influence of a natural fracture network on hydraulic fracture propagation in carbonate formations. Rock. Mech. Rock. Eng. 47, 575–587.
Liu, Z.Y., Pan, Z.J., Li, S.B., Zhang, L.G., Wang, F.S., Han, L.L., Zhang, J., Ma, Y.Y., Li, H., Li, W., 2022. Study on the effect of cemented natural fractures on hydraulic fracture propagation in volcanic reservoirs. Energy 241, 122845.

Lyu, S.F., Wang, S.W., Chen, X.J., Wang, S.F., Wang, T., Shi, X.H., Dong, Q.X., Li, J.Y., 2020. Natural fractures in soft coal seams and their effect on hydraulic fracture propagation: A field study. J. Pet. Sci. Eng. 192, 107255.
McDermott, C.I., Fraser-Harris, A., Sauter, M., Couples, G.D., Edlmann, K., Kolditz, O., Lightbody, A., Somerville, J., Wang, W., 2018. New experimental equipment re-creating geo-reservoir conditions in large, fractured, porous samples to investigate coupled thermal, hydraulic and polyaxial stress processes. Sci. Rep. 8, 14549.
Mollaali, M., Ziaei-Rad, V., Shen, Y.X., 2019. Numerical modeling of CO_2 fracturing by the phase field approach. J. Nat. Gas. Sci. Eng. 70, 102905.
Mou, P.W., Pan, J.N., Wang, K., Wei, J., Yang, Y.H., Wang, X.L., 2021. Influences of hydraulic fracturing on microfractures of high-rank coal under different in-situ stress conditions. Fuel 287, 119566.
Ohtani, H., Mikada, H., Takekawa, J., 2017. Fundamental research on the role of differential stress in hydraulic fracturing in strength-anisotropic medium. *21st Int. Symp. Recent Adv. Explor. Geophys.* 23, 1–6.
Pan, J.N., Mou, P.W., Ju, Y.W., Wang, K., Zhu, Q.Z., Ge, T.Y., Yu, K., 2022. Micro-nano-scale pore stimulation of coalbed methane reservoirs caused by hydraulic fracturing experiments. J. Pet. Sci. Eng. 214, 110512.
Paul, S., Chatterjee, R., 2011. Mapping of cleats and fractures as an indicator of in-situ stress orientation, Jharia Coalfield, India. Int J. Coal Geol. 88, 113–122.
Sherratt, J., Haddad, A.S., Wejzerowski, F., Rafati, R., 2021. Optimising well orientation in hydraulic fracturing of naturally fractured shale gas formations. J. Nat. Gas. Sci. Eng. 94, 104141.
Sherratt, J., Haddad, A.S., Rafati, R., 2023. Modifying the orientation of hydraulically fractured wells in tight reservoirs: the effect of in-situ stresses and natural fracture toughness. Geomech. Energy Envir 36, 100507.
Shimizu, H., Murata, S., Ishida, T., 2011. The distinct element analysis for hydraulic fracturing in hard rock considering fluid viscosity and particle size distribution. Int J. Rock. Mech. Min. Sci. 48, 712–727.
Silva, B.G.D., Einstein, H.H., 2014. Finite element study of fracture initiation in flaws subject to internal fluid pressure and vertical stress. Int J. Solids Struct. 51, 4122–4136.
Sun, X., Zhang, S.C., Ma, X.F., Zou, Y.S., Lin, G.Y., 2019. Experimental investigation on propagation behavior of hydraulic fractures in coal seam during refracturing. Geofluids 2, 1–15.
Taghichian, A., Hashemalhoseini, H., Zaman, M., Yang, Z., 2018. Geomechanical optimization of hydraulic fracturing in unconventional reservoirs: a semi-analytical approach. Int J. Fract. 213, 107–138.
Teng, J., Yao, Y.B., Liu, D.M., Cai, Y.D., 2015. Evaluation of coal texture distributions in the southern Qinshui basin, North China: investigation by a multiple geophysical logging method. Int J. Coal Geol. 140, 9–22.
Tingay, M.R.P., Hillis, R.R., Swarbrick, R.E., Morley, C.K., Damit, A.R., 2009. Origin of overpressure and pore-pressure prediction in the Baram province, Brunei. AAPG Bull. 93, 51–74.
Ulrich, N., Kirchner, V., Drucker, R., Wright, J.R., McLimans, C.J., Hazen, T.C., Campa, M.F., Grant, C.J., Lamendella, R., 2018. Response of aquatic bacterial communities to hydraulic fracturing in Northwestern Pennsylvania: a five-year study. Sci. Rep. -UK 8, 5683.
Vishkai, M., Gates, I., 2019. On multistage hydraulic fracturing in tight gas reservoirs: montney Formation, Alberta, Canada. J. Pet. Sci. Eng. 174, 1127–1141.
Wang, H., Yao, Y.B., Liu, D.M., Pan, Z.J., Yang, Y.H., Cai, Y.D., 2016. Fault-sealing capability and its impact on coalbed methane distribution in the Zhengzhuang field, southern Qinshui Basin, North China. J. Nat. Gas. Sci. Eng. 28, 613–625.
Wang, H., Yao, Y.B., Huang, C.C., Liu, D.M., Cai, Y.D., 2021b. Fault development characteristics and their effects on current gas content and productivity of No. 3 coal seam in the Zhengzhuang field, Southern Qinshui Basin, North China. Energy Fuels 35, 2268–2281.
Wang, M.Y., Gan, Q., Wang, T., Ma, Y.Q., Yan, C.Z., Benson, P., Wang, X.G., Elsworth, D., 2024. Propagation and complex morphology of hydraulic fractures in lamellar shales based on finite-discrete element modeling. Geomech. Geophys Geo 10, 1–22.
Wang, R., Pan, J.N., Wang, Z.Z., Li, G.F., Ge, T.Y., Zheng, H.D., Wang, X.L., 2021a. Influence of in situ stress on well test permeability and hydraulic fracturing of the Fanzhuang block, Qinshui Basin. Energy Fuels 35, 2121–2133.
Wang, T., Hu, W.R., Elsworth, D., Zhou, W., Zhou, W.B., Zhao, X.Y., Zhao, L.Z., 2017. The effect of natural fractures on hydraulic fracturing propagation in coal seams. J. Pet. Sci. Eng. 150, 180–190.
Wang, W., Zhao, Y.X., Sun, Z., Lu, C.S., 2021c. Effects of bedding planes on the fracture characteristics of coal under dynamic loading. Eng. Fract. Mech. 250, 107761.
Wei, J.G., Huang, S.P., Hao, G.W., Li, J.T., Zhou, X.F., Gong, T., 2020. A multi-perforation staged fracturing experimental study on hydraulic fracture initiation and propagation. Energ. Explor Exploit 38, 2466–2484.
Yan, C.Z., Wang, Y.X., Xie, X., Ali, S., Sheng, Z.G., 2023a. A 2D continuous-discrete mixed seepage model considering the fluid exchange and the pore pressure discontinuity across the fracture for simulating fluid-driven fracturing. Acta Geotech. 18, 5791–5810.
Yan, C.Z., Zhao, Z.H., Yang, Y., Zheng, H., 2023b. A three-dimensional thermal-hydro-mechanical coupling model for simulation of fracturing driven by Multiphysics. Comput. Geotech. 155, 105162.
Zhang, J., Roegiers, J.C., 2010. Discussion on “integrating borehole breakout dimensions, strength criteria, and leak-off test results, to constrain the state of stress across the Chelungpu Fault, Taiwan. Tectonophysics 492, 295–298.
Zhang, K.P., Chen, M., Wang, S.G., Li, J.X., Taufiqurrahman, M., 2022. Significant effect of the rock parameters of Longmaxi formation in hydraulic fracturing. Geomech. Energy Environ. 32, 100384.
Zhao, H.F., Liu, C.S., Xiong, Y.G., Zhen, H.B., Li, X.J., 2022c. Experimental research on hydraulic fracture propagation in group of thin coal seams. J. Nat. Gas. Sci. Eng. 103, 104614.
Zhao, P., Xie, L.Z., Fan, Z.C., Deng, L., Liu, J., 2021. Mutual interference of layer plane and natural fracture in the failure behavior of shale and the mechanism investigation. Pet. Sci. 18, 618–640.
Zhao, P., He, B., Zhang, B., Liu, J., 2022a. Porosity of gas shale: Is the NMR-based measurement reliable? Pet. Sci. 19, 509–517.
Zhao, Y., Zhang, Y.F., Wang, C.L., Liu, Q., 2022b. Hydraulic fracturing characteristics and evaluation of fracturing effectiveness under different anisotropic angles and injection rates: An experimental investigation in absence of confining pressure. J. Nat. Gas. Sci. Eng. 97, 104343.
Zhou, J., Chen, M., Jin, Y., Zhang, G.Q., 2008. Analysis of fracture propagation behavior and fracture geometry using a tri-axial fracturing system in naturally fractured reservoirs. Int J. Rock. Mech. Min. Sci. 45, 1143–1152.
Zou, J.P., Jiao, Y.Y., Tan, F., Lv, J.H., Zhang, Q.Y., 2021. Complex hydraulic-fracture-network propagation in a naturally fractured reservoir. Comput. Geotech. 135, 104165.
Zou, M.J., Wei, C.T., Pan, H.Y., Sesay, K.S., Cao, J., 2010. Productivity of coalbed methane wells in southern of Qinshui Basin. Min. Sci. Technol. 20, 765–769.
Zou, Y.S., Ma, X.F., Zhang, S.C., Zhou, T., Li, H., 2016. Numerical investigation into the influence of bedding plane on hydraulic fracture network propagation in shale formations. Rock. Mech. Rock. Eng. 49, 3597–3614.